Modulated solar pressure-based surface shape control of paraboloid space reflectors with an off-axis Sun-line

Jiafu Liu[1*], Colin R McInnes[2]

[1] Department of Aerospace Engineering, Shenyang Aerospace University, Shenyang, 110136, China

[2] School of Engineering, University of Glasgow, Glasgow G12 8QQ, UK

E-mail: liujiafuericking@163.com

Abstract: This paper considers utilizing solar radiation pressure (SRP) to actively control the surface shape of a reflector consisting of a rigid hoop and slack membrane with embedded reflectivity control devices (RCDs). The full nonlinear static partial differential governing equations for a reflector with negligible elastic deformations are established for the circumferential, radial and transverse directions respectively, in which the SRP force with ideal /non-perfect models, the centripetal force caused by the rotation of the reflector and the internal stresses are considered. The inverse problem is then formulated by assuming that the required surface shape is known, and then the governing algebraic-differential equations used to determine the required surface reflectivity, together with the internal stresses where are presented accordingly. The validity of the approach is verified by comparing the results in this paper with corresponding published results as benchmarks. The feasible regions of the angular velocity and Sun angle for a paraboloidal reflector with an invariant radius and focal length (case 1), and the achievable focal lengths with a specific angular velocity and Sun angle (case 2) are presented for two SRP models respectively, both by considering the constraints on the reflectivity and internal stresses. It is then found that the feasible region is toward a larger angular velocity and Sun angle when using the non-perfect SRP model, compared with the ideal one in case 1. The angular velocity of the spinning reflector should be within a certain range to make the required reflectivity profiles within a practical range, i.e., [0, 0.88], as indicated from prior NASA solar sail studies. In case 2, it is found that the smallest achievable focal length of the reflector with the non-perfect SRP model is smaller than that with the ideal SRP model. It is also found that the stress level is extremely low for all cases considered and that the typical real material strength available for the reflector is sufficient to withstand these internal stresses.

Keywords: Paraboloid space reflectors, reflectivity control devices, solar radiation pressure, inverse analysis

1. Introduction

Extremely large and lightweight membrane structures have been researched for use as reflectors with a high area-to-mass ratio which can be folded and stowed within a small volume and thus can be launched at low cost [1]. The range of applications of this type of structure includes solar sails [2], radio-frequency (RF) communication antennae [3], scientific telescopes [4] and solar power satellites [5]. It was also reported that this type of structure can be used as a solar concentrator to sublimate asteroid material [6]. The surface shape control for such membranes is

one of the most important and interesting research topics for gossamer structures.

Once delivered into orbit, the membrane can be deployed either by rigid support booms with joints or by continuous flexible inflatable booms [7, 8]. The latter may be a better and more attractive choice because of its lower weight and simpler configuration. The solar reflector usually consists of a large membrane and hoop structure as shown in Fig. 1(a). The hoop can be inflated and then rigidized immediately when deployed in orbit [9]. In this paper, reflectivity control devices (RCDs) are considered as the actuators for controlling the shape of the slack membrane actively. RCDs are coated on the surface of the membrane and their reflectivity can be modulated within a certain range [10, 11]. The effectiveness of RCDs for engineering applications was verified by the IKAROS solar sails project [10], and the feasibility of adopting RCDs for orbit [12] and/or attitude control [13] of solar sails was investigated numerically. It was demonstrated in [11] that the natural shape of the membrane supported by the hoop and displaced by solar radiation pressure can never be a paraboloid if the reflectivity is constant. However, it was then demonstrated that by a suitable choice of reflectivity profile across the reflector, a true paraboloid could be generated, assuming that the Sun-line is along the axis of symmetry of the paraboloid. This paper extends the work of [11] to the much more complex case of a paraboloid reflector with an off-axis Sun-line, as discussed later.

Concerning the surface correction/control of the membrane, a review has been provided in [14]. By manipulating the temperature across the structure, the static shape of a space antenna reflector can be controlled with an analytical procedure presented in [15]. For an inflatable structure the required profile can also be controlled by enforced boundary displacements [16]. In [17], pressurised lenticular structures with transparent canopies were proposed to control an optical membrane reflector to be a paraboloid. The effectiveness of dielectric elastomer actuators for accurate shape control of lightweight flexible aperture mirrors was verified numerically and experimentally in [18]. In solar sail ground experiments, piezoceramic macro-fiber composites were adopted to control the out-of-plane displacement of the solar sail membrane [19]. Recently, the required shape of a solar collector has been considered to be controlled using shape memory alloy actuators, which have advantages over other smart materials as discussed in [20]. Advanced materials such as polyvinylidene fluoride (PVDF) based piezopolymer actuators were developed to precisely control the surface of membrane reflectors [21]. Electroactive materials are usually proposed for structural vibration control and piezoceramic wafers were proposed to be attached in a bimorph configuration near the boundary of a membrane mirror structure to correct the shape error and eliminate vibrations [22]. Piezoceramic PZT (lead zirconate titanate) actuators were suggested to be used for correcting surface errors of flexible mirrors and thermal distortions [23]. In this paper the proposed RCD-based shape control of a solar reflector utilizing modulation of the SRP force to correct the surface of the reflector will be considered.

Previous research on space reflector shape control using modulation of the SRP force can be found in [11, 24]. The elastic deformations of a flexible membrane with large transverse displacements are analyzed and the required reflectivity within the reflector is determined to form a paraboloid shape [24]. It is found that the smallest achievable focal length is however rather large. A much smaller focal length can be obtained when a slack membrane is used to construct a solar reflector [11]. The authors concluded that the reflector in [11] should be exploited in future because much smaller focal lengths can be achieved in [11] than those in [24]. In [11], the authors analyzed the case when the Sun-line was perpendicular to the hoop plane using an ideal SRP

model. This paper will relax the above-mentioned restrictions, i.e., considering the case when the Sun-line is off-axis based on a non-perfect SRP force model. It is also noted that the elastic strain of a 100 m-diameter flexible reflector is of the order of 10^{-5}, as noted in Fig. 10 from [24]. This extremely small strain makes it acceptable to perform the surface shape control of a slack reflector membrane without considering its elasticity.

In this paper, a more general analysis will be performed based on [11] and some restrictions in [11] will be relaxed. First, the full nonlinear partial differential governing equations in the circumferential, radial and transverse directions are derived for the solar reflector. The modulated SRP force, internal tensions and centripetal force are then considered. The ideal and non-perfect SRP force models are also used and, importantly, the condition of an off-axis Sun-line is considered. Secondly, the inverse problem is presented, i.e., the shape of the reflector is taken as a paraboloid and the required reflectivity profile is sought. The nonlinear coupled partial differential and algebric equations for the internal stresses and reflectivity are again used for the ideal and non-perfect SRP force models respectively. Thirdly, for the ideal and non-perfect SRP force models, we present the feasible regions for the reflector spin rate and Sun angle for a paraboloid reflector. The differences between the feasible regions for the two SRP models are identified and discussed in some detail. The feasible regions for the radius and focal length for a paraboloid reflector with a constant spin rate and Sun angle are also provided for the two models. The aforementioned feasible regions are calculated by considering the reflectivity and internal stresses within physically realizable ranges. The magnitude of the stress level is presented in the analysis and the corresponding conclusions are given.

2. Equilibrium conditions

The basic structure and configuration of the solar reflector is presented in Fig. 1 (a). The rigid hoop is the support structure and the slack membrane will be controlled to be a paraboloid shape for applications as a reflector, as discussed in Section 1. A reference frame $Oxyz$ is established with its origin O at the center of the circular hoop plane, where Oz is perpendicular to the hoop plane, Ox is selected to make the Sun-line vector $\boldsymbol{S}$ lie within Oxz, and Oy forms a right-handed triad. One can note that Oxy is the hoop plane. The reflector can rotate with an angular velocity ω about Oz. E is on the reflector and "O" is the projected point of E on to Oxy. One can then select two arbitrary infinitely close points on the edge of the hoop denoted as E_1 and E_2 respectively. One can then establish another reference frame $O\xi\eta z$ with $O\xi$ coincident with the projected line of the curve EE_2 on to Oxy and $O\eta$ forms a right-handed triad with $O\xi$ and Oz. A and A_3 are two arbitrary infinitely close points on the curve EE_2 with A' and A_3' representing the corresponding projected points on to Oxy respectively. A_1 is on the curve EE_1 and should be selected to make $A'A_1'$ perpendicular to $O\xi$ with A_1' representing the projected point of A' on to Oxy. Finally, one should select A_2 on the curve EE_1 to make the projected shape of $AA_1A_2A_3$ denoted as Σ onto Oxy a rectangular shape $A'A_1'A_2'A_3'$ denoted as Σ' with A_2' representing the projection of the point A_2 on to Oxy. One can note that the infinitesimal element Σ is used for establishing the static equilibrium equations and Σ' is an auxiliary element used to facilitate the analysis. Subsequent analysis will be used to establish the static equilibrium equations for Σ by using Σ' in a later section.

Figure 1(a) presents the diagrammatic sketch of Σ and Σ' along with the configuration of the reflector. Meanwhile, the partial enlarged figure of Σ and Σ' is also presented to make them clearer.

Figure 1(b) shows the relationship between *Oxyz* and *Oξηz*, and Σ' with $d\xi$ and $d\eta$ representing the side lengths. In Fig. 1(c), both Σ and Σ' are given to make the relation between them clear. Moreover, the stresses along each side of Σ are also presented.

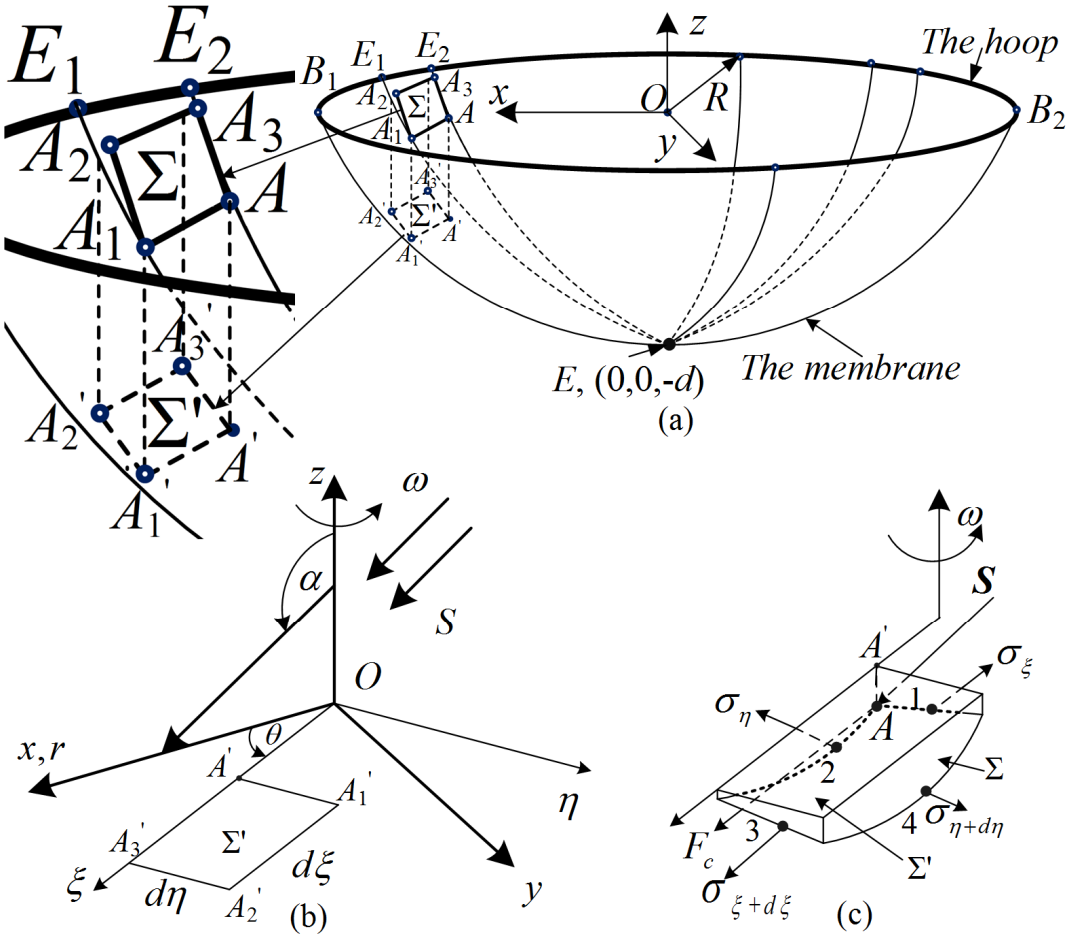

Fig. 1. (a) The basic configuration of the reflector, the infinitesimal element Σ and its projection Σ' and a partial enlarged figure, (b) Two coordinate reference frames, (c) The arbitrary infinitesimal element for determining the stresses and reflectivity

It is evident that the internal stresses and the required reflectivity at A can be obtained when $d\xi$ and $d\eta$ approach 0. The position of A' can be determined by the radial position ξ and angle θ. It is evident that the rotational transformation from *Oxyz* to *Oξηz* can be realized by one rotation, the rotation matrix $\mathbf{A}_{d2r}$ and is as follows.

$$\mathbf{A}_{d2r} = \begin{bmatrix} \cos\theta & \sin\theta & 0 \\ -\sin\theta & \cos\theta & 0 \\ 0 & 0 & 1 \end{bmatrix} \tag{1}$$

The area of Σ is then calculated as follows

$$dS = \sqrt{1+\left(z'_{\xi}\right)^2+\left(z'_{\eta}\right)^2}\, d\xi d\eta \tag{2}$$

where z is the z displacement component of A relative to O, and the superscript prime together with the subscripts ξ and η represent the partial derivatives with respect to ξ and η respectively. The centripetal force F_c can also be calculated as follows

$$F_c = \omega^2 \xi \tau dS \tag{3}$$

where τ is the membrane areal density and ω is the angular velocity of the spinning solar reflector.

The components of the Sun-line vector $\boldsymbol{S}$ in $Oxyz$ and $O\xi\eta z$ can be expressed as follows

$$\boldsymbol{S}_d = \begin{bmatrix} \sin\alpha \\ 0 \\ \cos\alpha \end{bmatrix}_d, \qquad \boldsymbol{S}_r = \mathbf{A}_{d2r}\boldsymbol{S}_d = \begin{bmatrix} \cos\theta\sin\alpha \\ -\sin\theta\sin\alpha \\ \cos\alpha \end{bmatrix}_r \tag{4}$$

where the subscripts d and r represent the components in $Oxyz$ and $O\xi\eta z$ respectively. The components of the normal vector of the solar reflector $\boldsymbol{n}$ at A, in $O\xi\eta z$, are as follows.

$$\boldsymbol{n} = \left[1+\left(z'_\xi\right)^2+\left(z'_\eta\right)^2\right]^{-1/2}\begin{bmatrix} z'_\xi \\ z'_\eta \\ -1 \end{bmatrix}_r \tag{5}$$

A more exact model of the SRP force is considered instead of the ideal model frequently used, where the reflectance, absorption and emissivity of the reflector film are considered [25]. The expression of the normal and transverse components of the SRP force experienced by Σ or dS within the solar reflector is given by

$$\begin{cases} \boldsymbol{F}_n = \kappa P dS\left[\left(1+\rho\bar{s}\right)\cos^2\psi + B_f(1-\bar{s})\rho\cos\psi + (1-\rho)\dfrac{\varepsilon_f B_f - \varepsilon_b B_b}{\varepsilon_f+\varepsilon_b}\cos\psi\right]\boldsymbol{n} \\ \boldsymbol{F}_t = \kappa P dS\left(1-\rho\bar{s}\right)\cos\psi\sin\psi\boldsymbol{t} \end{cases} \tag{6}$$

where P is the nominal solar radiation pressure constant at 1 astronomical unit (AU) from the Sun, adopted as $4.56\times10^{-6}N/m^2$, $\kappa=(R_0/R_s)^2$, R_0=1AU and R_s denotes the distance between the solar reflector and the Sun. Then dS is the infinitesimal surface element as shown in Fig. 2. It is assumed that the solar reflector is at 1AU from the Sun without loss of generality. Moreover, $\boldsymbol{n}$ and $\boldsymbol{t}$ indicate the normal and transverse unit vectors in the preceding equation as shown in Fig. 2. In addition ρ is the reflectivity coefficient of the incident solar photons, which will be determined as the (constrained) control input in this paper, $\bar{s}$ is the specular reflection coefficient, B_f and B_b are the non-Lambertian coefficients for the front and back surfaces, and ε_f and ε_b are front and back surface emissivity coefficients. One can find these optical parameters in [25], where ρ_{max}=0.88, $\bar{s}=0.94$, ε_f=0.05, ε_b=0.55, B_f=0.79 and B_b=0.55 so that the force components can be written as

$$\begin{cases} \boldsymbol{F}_n = PdS\cos\psi\left(\cos\psi + C_{c2}\right)\boldsymbol{n} + \rho\left(\bar{s}\cos\psi + C_{1m2}\right)PdS\cos\psi\boldsymbol{n} \\ \boldsymbol{F}_t = PdS\cos\psi\sin\psi\boldsymbol{t} - \rho\bar{s}PdS\cos\psi\sin\psi\boldsymbol{t} \end{cases}$$
$$C_{c1} = B_f(1-\bar{s}), C_{c2} = \frac{\varepsilon_f B_f - \varepsilon_b B_b}{\varepsilon_f+\varepsilon_b}, C_{1m2} = C_{c1} - C_{c2} \tag{7}$$

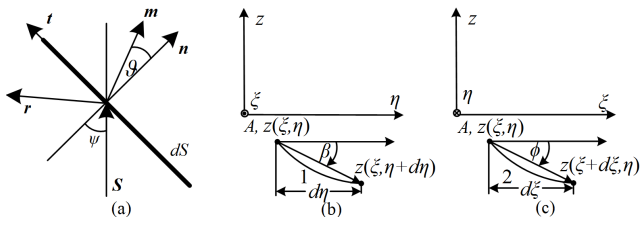

Fig.2. (a) The solar radiation pressure force model, (b, c) geometry of the edges of the infinitesimal element Σ

where the unit vector $\boldsymbol{r}$ is the direction of the specularly reflected photons, $\boldsymbol{m}$ is the unit vector in the direction of the total SRP force and ϑ is the angle between $\boldsymbol{m}$ and $\boldsymbol{n}$.

For the selected infinitesimal element Σ, cosψ is calculated as follows.

$$\cos\psi = \left[1+\left(z_\xi^{'}\right)^2+\left(z_\eta^{'}\right)^2\right]^{-1/2}\left(z_\xi^{'}\cos\theta\sin\alpha - z_\eta^{'}\sin\theta\sin\alpha - \cos\alpha\right) \tag{8}$$

The following expression then holds for the infinitesimal element Σ.

$$\begin{aligned}
&\left(\sin\psi\right)\boldsymbol{t} = \boldsymbol{n}\times\left(\boldsymbol{S}\times\boldsymbol{n}\right)\\
&= \left[1+\left(z_\xi^{'}\right)^2+\left(z_\eta^{'}\right)^2\right]^{-1}\begin{bmatrix}\cos\theta\sin\alpha + z_\xi^{'}\cos\alpha + \left(z_\eta^{'}\right)^2\cos\theta\sin\alpha + z_\xi^{'}z_\eta^{'}\sin\theta\sin\alpha\\ z_\eta^{'}\cos\alpha - \sin\theta\sin\alpha - z_\xi^{'}z_\eta^{'}\cos\theta\sin\alpha - \left(z_\xi^{'}\right)^2\sin\theta\sin\alpha\\ \left(z_\eta^{'}\right)^2\cos\alpha - z_\eta^{'}\sin\theta\sin\alpha + \left(z_\xi^{'}\right)^2\cos\alpha + z_\xi^{'}\cos\theta\sin\alpha\end{bmatrix}\\
&= \left[1+\left(z_\xi^{'}\right)^2+\left(z_\eta^{'}\right)^2\right]^{-1}\begin{bmatrix}f_{t\xi}\\ f_{t\eta}\\ f_{tz}\end{bmatrix}
\end{aligned} \tag{9}$$

Thus, the normal and transverse components of the SRP force in $O\xi\eta z$ can be expressed as follows by substituting Eqs. (5, 9) into Eq. (7).

$$\begin{cases}
F_{n\xi} = Pz_\xi^{'}\cos\psi\left(\cos\psi + C_{c2}\right)d\xi d\eta + \rho z_\xi^{'}\left(\bar{s}\cos\psi + C_{1m2}\right)P\cos\psi d\xi d\eta\\
F_{n\eta} = Pz_\eta^{'}\cos\psi\left(\cos\psi + C_{c2}\right)d\xi d\eta + \rho z_\eta^{'}\left(\bar{s}\cos\psi + C_{1m2}\right)P\cos\psi d\xi d\eta\\
F_{nz} = -P\cos\psi\left(\cos\psi + C_{c2}\right)d\xi d\eta - \rho\left(\bar{s}\cos\psi + C_{1m2}\right)P\cos\psi d\xi d\eta
\end{cases}$$

$$\begin{cases}
F_{t\xi} = Pf_{t\xi}\cos\psi\left[1+\left(z_\xi^{'}\right)^2+\left(z_\eta^{'}\right)^2\right]^{-1/2}d\xi d\eta - \rho\bar{s}Pf_{t\xi}\cos\psi\left[1+\left(z_\xi^{'}\right)^2+\left(z_\eta^{'}\right)^2\right]^{-1/2}d\xi d\eta\\
F_{t\eta} = Pf_{t\eta}\cos\psi\left[1+\left(z_\xi^{'}\right)^2+\left(z_\eta^{'}\right)^2\right]^{-1/2}d\xi d\eta - \rho\bar{s}Pf_{t\eta}\cos\psi\left[1+\left(z_\xi^{'}\right)^2+\left(z_\eta^{'}\right)^2\right]^{-1/2}d\xi d\eta\\
F_{tz} = Pf_{tz}\cos\psi\left[1+\left(z_\xi^{'}\right)^2+\left(z_\eta^{'}\right)^2\right]^{-1/2}d\xi d\eta - \rho\bar{s}Pf_{tz}\cos\psi\left[1+\left(z_\xi^{'}\right)^2+\left(z_\eta^{'}\right)^2\right]^{-1/2}d\xi d\eta
\end{cases} \tag{10}$$

Then the internal tensions at each edge will be derived by referring to Fig. 1. The internal resultant force T_ξ and its ξ and z components denoted as $T_{\xi\xi}$ and $T_{\xi z}$ for curve 1 are as follows

$$\begin{aligned}
&T_\xi = \sigma_\xi\sqrt{1+\left(z_\eta^{'}\right)^2}\,d\eta\\
&T_{\xi\xi} = \sigma_\xi\sqrt{1+\left(z_\eta^{'}\right)^2}\,d\eta\cos\phi, \qquad T_{\xi z} = \sigma_\xi\sqrt{1+\left(z_\eta^{'}\right)^2}\,d\eta\sin\phi
\end{aligned} \tag{11}$$

where σ_ξ is the stress as shown in Fig. 1, $\sqrt{1+\left(z_\eta^{'}\right)^2}\,d\eta$ is the length of curve 1, ϕ is the angle as shown in Fig. 2(c), and tanϕ, cosϕ and sinϕ are defined as follows.

$$\tan\phi = z_\xi^{'}, \cos\phi = \left[1+\left(z_\xi^{'}\right)^2\right]^{-1/2}, \sin\phi = z_\xi^{'}\left[1+\left(z_\xi^{'}\right)^2\right]^{-1/2} \tag{12}$$

Similarly, the internal resultant force $T_{\xi+d\xi}$ and its ξ and z components denoted as $T_{\xi+d\xi,\,\xi}$ and

$T_{\xi+d\xi,\,z}$ for curve 3 are as follows.

$$
\begin{aligned}
T_{\xi+d\xi} &= \left(\sigma_\xi + \frac{\partial \sigma_\xi}{\partial \xi} d\xi\right)\sqrt{1+\left(z_\eta^{'}\right)^2}\, d\eta \\
T_{\xi+d\xi,\xi} &= T_{\xi+d\xi}\cos\left(\phi + \frac{\partial \phi}{\partial \xi} d\xi\right) = \left(\cos\phi - \frac{\partial \phi}{\partial \xi} d\xi \sin\phi\right)\left(\sigma_\xi + \frac{\partial \sigma_\xi}{\partial \xi} d\xi\right)\sqrt{1+\left(z_\eta^{'}\right)^2}\, d\eta \\
T_{\xi+d\xi,z} &= T_{\xi+d\xi}\sin\left(\phi + \frac{\partial \phi}{\partial \xi} d\xi\right) = \left(\sin\phi + \frac{\partial \phi}{\partial \xi} d\xi \cos\phi\right)\left(\sigma_\xi + \frac{\partial \sigma_\xi}{\partial \xi} d\xi\right)\sqrt{1+\left(z_\eta^{'}\right)^2}\, d\eta
\end{aligned}
\tag{13}
$$

In the preceding equations, the variations of σ_ξ and ϕ are considered. The internal resultant force T_η and its η and z components denoted as $T_{\eta\eta}$ and $T_{\eta z}$ for curve 2 are as follows

$$
\begin{aligned}
T_\eta &= \sigma_\eta \sqrt{1+\left(z_\xi^{'}\right)^2}\, d\xi \\
T_{\eta\eta} &= \sigma_\eta \sqrt{1+\left(z_\xi^{'}\right)^2}\, d\xi \cos\beta, \qquad T_{\eta z} = \sigma_\eta \sqrt{1+\left(z_\xi^{'}\right)^2}\, d\xi \sin\beta
\end{aligned}
\tag{14}
$$

where tanβ, cosβ and sinβ are defined as follows by observing Fig. 2(b).

$$
\tan\beta = z_\eta^{'}, \cos\beta = \left[1+\left(z_\eta^{'}\right)^2\right]^{-1/2}, \sin\beta = z_\eta^{'}\left[1+\left(z_\eta^{'}\right)^2\right]^{-1/2} \tag{15}
$$

Similarly, the internal resultant force $T_{\eta+d\eta}$ and its η and z components denoted as $T_{\eta+d\eta,\,\eta}$ and $T_{\eta+d\eta,\,z}$ for curve 4 are as follows.

$$
\begin{aligned}
T_{\eta+d\eta} &= \left(\sigma_\eta + \frac{\partial \sigma_\eta}{\partial \eta} d\eta\right)\sqrt{1+\left(z_\xi^{'}\right)^2}\, d\xi \\
T_{\eta+d\eta,\eta} &= \left(\sigma_\eta + \frac{\partial \sigma_\eta}{\partial \eta} d\eta\right)\sqrt{1+\left(z_\xi^{'}\right)^2}\, d\xi\left(\cos\beta - \frac{\partial \beta}{\partial \eta} d\eta \sin\beta\right) \\
T_{\theta+d\theta,z} &= \left(\sigma_\eta + \frac{\partial \sigma_\eta}{\partial \eta} d\eta\right)\sqrt{1+\left(z_\xi^{'}\right)^2}\, d\xi\left(\sin\beta + \frac{\partial \beta}{\partial \eta} d\eta \cos\beta\right)
\end{aligned}
\tag{16}
$$

In the preceding equations, the variations of σ_η and β are considered. The equilibrium equation along the ξ direction can be expressed as follows by considering the related force components.

$$
\begin{aligned}
&-\sigma_\xi \cos\phi\sqrt{1+\left(z_\eta^{'}\right)^2}\, d\eta + \left(\cos\phi - \frac{\partial \phi}{\partial \xi} d\xi \sin\phi\right)\left[\sigma_\xi + \frac{\partial \sigma_\xi}{\partial \xi} d\xi\right]\sqrt{1+\left(z_\eta^{'}\right)^2}\, d\eta \\
&+\omega^2 \xi\tau\sqrt{1+\left(z_\xi^{'}\right)^2+\left(z_\eta^{'}\right)^2}\, d\xi d\eta + P z_\xi^{'}\cos\psi\left(\cos\psi + C_{c2}\right) d\xi d\eta + \rho z_\xi^{'}\left(\overline{s}\cos\psi + C_{1m2}\right) P\cos\psi\, d\xi d\eta \\
&+P f_{t\xi}\cos\psi\left[1+\left(z_\xi^{'}\right)^2+\left(z_\eta^{'}\right)^2\right]^{-1/2} d\xi d\eta - \rho\overline{s} P f_{t\xi}\cos\psi\left[1+\left(z_\xi^{'}\right)^2+\left(z_\eta^{'}\right)^2\right]^{-1/2} d\xi d\eta = 0
\end{aligned}
\tag{17}
$$

The final governing partial differential equation (PDE) for the ξ-axis is then given as follows

$$\sqrt{1+\left(z_\eta^{'}\right)^2}\left[1+\left(z_\xi^{'}\right)^2\right]^{-1/2}\frac{\partial\sigma_\xi}{\partial\xi}-\sqrt{1+\left(z_\eta^{'}\right)^2}\sigma_\xi z_\xi^{'}z_\xi^{''}\left[1+\left(z_\xi^{'}\right)^2\right]^{-3/2}+\omega^2\xi\tau\sqrt{1+\left(z_\xi^{'}\right)^2+\left(z_\eta^{'}\right)^2}$$
$$+Pz_\xi^{'}\cos\psi\left(\cos\psi+C_{c2}\right)+\rho Pz_\xi^{'}\cos\psi\left(\overline{s}\cos\psi+C_{1m2}\right)$$
$$+Pf_{t\xi}\cos\psi\left[1+\left(z_\xi^{'}\right)^2+\left(z_\eta^{'}\right)^2\right]^{-1/2}-\rho\overline{s}Pf_{t\xi}\cos\psi\left[1+\left(z_\xi^{'}\right)^2+\left(z_\eta^{'}\right)^2\right]^{-1/2}=0 \tag{18}$$

and the final PDEs governing the η and z directions are as follows respectively.

$$\sqrt{1+\left(z_\xi^{'}\right)^2}\frac{\partial\sigma_\eta}{\partial\eta}\left[1+\left(z_\eta^{'}\right)^2\right]^{-1/2}-\sqrt{1+\left(z_\xi^{'}\right)^2}\sigma_\eta z_\eta^{'}z_\eta^{''}\left[1+\left(z_\eta^{'}\right)^2\right]^{-3/2}$$
$$+Pz_\eta^{'}\cos\psi\left(\cos\psi+C_{c2}\right)+\rho z_\eta^{'}\left(\overline{s}\cos\psi+C_{1m2}\right)P\cos\psi \tag{19}$$
$$+Pf_{t\eta}\cos\psi\left[1+\left(z_\xi^{'}\right)^2+\left(z_\eta^{'}\right)^2\right]^{-1/2}-\rho\overline{s}Pf_{t\eta}\cos\psi\left[1+\left(z_\xi^{'}\right)^2+\left(z_\eta^{'}\right)^2\right]^{-1/2}=0$$

$$\sqrt{1+\left(z_\eta^{'}\right)^2}\frac{\partial\sigma_\xi}{\partial\xi}z_\xi^{'}\left[1+\left(z_\xi^{'}\right)^2\right]^{-1/2}+\sqrt{1+\left(z_\eta^{'}\right)^2}\sigma_\xi z_\xi^{''}\left[1+\left(z_\xi^{'}\right)^2\right]^{-1/2}$$
$$-\sqrt{1+\left(z_\eta^{'}\right)^2}\sigma_\xi\left(z_\xi^{'}\right)^2 z_\xi^{''}\left[1+\left(z_\xi^{'}\right)^2\right]^{-3/2}\sqrt{1+\left(z_\xi^{'}\right)^2}\frac{\partial\sigma_\eta}{\partial\eta}z_\eta^{'}\left[1+\left(z_\eta^{'}\right)^2\right]^{-1/2}$$
$$+\sqrt{1+\left(z_\xi^{'}\right)^2}\sigma_\eta z_\eta^{''}\left[1+\left(z_\eta^{'}\right)^2\right]^{-1/2}-\sqrt{1+\left(z_\xi^{'}\right)^2}\sigma_\eta\left(z_\eta^{'}\right)^2 z_\eta^{''}\left[1+\left(z_\eta^{'}\right)^2\right]^{-3/2} \tag{20}$$
$$-P\cos\psi\left(\cos\psi+C_{c2}\right)-\rho\left(\overline{s}\cos\psi+C_{1m2}\right)P\cos\psi$$
$$+Pf_{tz}\cos\psi\left[1+\left(z_\xi^{'}\right)^2+\left(z_\eta^{'}\right)^2\right]^{-1/2}-\rho\overline{s}Pf_{tz}\cos\psi\left[1+\left(z_\xi^{'}\right)^2+\left(z_\eta^{'}\right)^2\right]^{-1/2}=0$$

The results and discussion in the subsequent sections will be based on the general governing PDEs in Eqs. (18-20).

3. Shape control by reflectivity modulation

The basic idea in [11] is adopted in this paper where an inverse problem is formulated. The prescribed shape of the surface of the solar reflector is assumed to be a paraboloid and it is then determined how to modulate the reflectivity considering the physical restriction on reflectivity across the reflector and the requirement for neither negative nor over-large stresses within the reflector membrane.

The expression for the reference paraboloid is assumed as follows by referring to Fig. 1 so that

$$a\left(x^2+y^2\right)=z+d \tag{21}$$

where a and d are determined by the radius R of the hoop and the area S of the paraboloid. The relations are found from [11] as follows

$$d=aR^2 \tag{22a}$$

$$S = 2\pi \frac{\left(4R^2a^2+1\right)^{3/2}-1}{12a^2} \tag{22b}$$

where in practice R and S would be given. Here S is not given directly, but is defined as follows.

$$S = k\pi R^2 \left(k > 1\right) \tag{23}$$

It is clear that πR^2 is the area of the projected area of the solar reflector on to the hoop plane. The parameter a can be calculated for each given k by using Eq. (22). The following expressions then hold for the paraboloid solar reflector.

$$z_\xi^{'} = 2a\xi, z_\xi^{''} = 2a, \qquad z_\eta^{'} = 0, z_\eta^{''} = 0 \tag{24}$$

Therefore, all related expressions can be further simplified so that Eqs. (18-20) can be simplified as follows.

$$\begin{aligned}
&\frac{\partial \sigma_\xi}{\partial \xi} - \sigma_\xi z_\xi^{'} z_\xi^{''}\left[1+\left(z_\xi^{'}\right)^2\right]^{-1} + \omega^2\xi\tau\left[1+\left(z_\xi^{'}\right)^2\right] + Pf_{t\xi}\cos\psi - \rho\bar{s}Pf_{t\xi}\cos\psi \\
&+Pz_\xi^{'}\left[1+\left(z_\xi^{'}\right)^2\right]^{1/2}\cos\psi\left(\cos\psi + C_{c2}\right) + \rho Pz_\xi^{'}\left[1+\left(z_\xi^{'}\right)^2\right]^{1/2}\cos\psi\left(\bar{s}\cos\psi + C_{1m2}\right) = 0 \\
&\frac{\partial \sigma_\eta}{\partial \eta} + Pf_{t\eta}\cos\psi\left[1+\left(z_\xi^{'}\right)^2\right]^{-1} - \rho\bar{s}Pf_{t\eta}\cos\psi\left[1+\left(z_\xi^{'}\right)^2\right]^{-1} = 0 \\
&\frac{\partial \sigma_\xi}{\partial \xi} z_\xi^{'} + \sigma_\xi z_\xi^{''} - \sigma_\xi\left(z_\xi^{'}\right)^2 z_\xi^{''}\left[1+\left(z_\xi^{'}\right)^2\right]^{-1} + Pf_{tz}\cos\psi - \rho\bar{s}Pf_{tz}\cos\psi \\
&-P\cos\psi\left(\cos\psi + C_{c2}\right)\left[1+\left(z_\xi^{'}\right)^2\right]^{1/2} - \rho P\cos\psi\left(\bar{s}\cos\psi + C_{1m2}\right)\left[1+\left(z_\xi^{'}\right)^2\right]^{1/2} = 0
\end{aligned} \tag{25}$$

In the preceding three equations, one can see that three unknowns including σ_ξ, σ_η and ρ are to be solved for in the inverse problem.

It is evident that the radial and transverse equilibrium equations can be used to determine the radial stress σ_ξ and the reflectivity ρ. The σ_η equilibrium equation can be further written as follows.

$$\begin{aligned}
&\frac{\partial \sigma_\eta}{\partial \theta} - P\xi\sin\theta\sin\alpha\left[1+\left(z_\xi^{'}\right)^2\right]^{-1/2}\left(z_\xi^{'}\cos\theta\sin\alpha - \cos\alpha\right) \\
&+\rho\bar{s}P\xi\sin\theta\sin\alpha\left[1+\left(z_\xi^{'}\right)^2\right]^{-1/2}\left(z_\xi^{'}\cos\theta\sin\alpha - \cos\alpha\right) = 0
\end{aligned} \tag{26}$$

where $\partial\sigma_\xi/\partial\xi$ and ρ can be derived as follows by considering the first and third equations of Eq. (25) such that

$$\rho=\frac{\sigma_\xi z_\xi^{''}\left[1+\left(z_\xi^{'}\right)^2\right]^{-1}}{P\left(z_\xi^{'}\cos\theta\sin\alpha-\cos\alpha\right)\left(\overline{s}\left[1+\left(z_\xi^{'}\right)^2\right]^{-1/2}\left(z_\xi^{'}\cos\theta\sin\alpha-\cos\alpha\right)+C_{1m2}\right)}$$

$$-\frac{\left(\left[1+\left(z_\xi^{'}\right)^2\right]^{-1/2}\left(z_\xi^{'}\cos\theta\sin\alpha-\cos\alpha\right)+C_{c2}\right)}{\left(\overline{s}\left[1+\left(z_\xi^{'}\right)^2\right]^{-1/2}\left(z_\xi^{'}\cos\theta\sin\alpha-\cos\alpha\right)+C_{1m2}\right)}$$

$$-\frac{\omega^2\xi\tau z_\xi^{'}}{P\left(z_\xi^{'}\cos\theta\sin\alpha-\cos\alpha\right)\left\{\overline{s}\left[1+\left(z_\xi^{'}\right)^2\right]^{-1/2}\left(z_\xi^{'}\cos\theta\sin\alpha-\cos\alpha\right)+C_{1m2}\right\}}$$

$$\frac{\partial\sigma_\xi}{\partial\xi}=\frac{z_\xi^{''}s\sigma_\xi\left[1+\left(z_\xi^{'}\right)^2\right]^{-3/2}\left(\cos\theta\sin\alpha+z_\xi^{'}\cos\alpha\right)}{\left\{\overline{s}\left[1+\left(z_\xi^{'}\right)^2\right]^{-1/2}\left(z_\xi^{'}\cos\theta\sin\alpha-\cos\alpha\right)+C_{1m2}\right\}}$$

$$-\frac{z_\xi^{'}s\omega^2\xi\tau\left[1+\left(z_\xi^{'}\right)^2\right]^{-1/2}\left(\cos\theta\sin\alpha+z_\xi^{'}\cos\alpha\right)}{\left\{\overline{s}\left[1+\left(z_\xi^{'}\right)^2\right]^{-1/2}\left(z_\xi^{'}\cos\theta\sin\alpha-\cos\alpha\right)+C_{1m2}\right\}}-\omega^2\xi\tau$$

$$-\frac{sP\left(\cos\theta\sin\alpha+z_\xi^{'}\cos\alpha\right)\left(z_\xi^{'}\cos\theta\sin\alpha-\cos\alpha\right)\left(\left[1+\left(z_\xi^{'}\right)^2\right]^{-1/2}\left(z_\xi^{'}\cos\theta\sin\alpha-\cos\alpha\right)+C_{c2}\right)}{\left(\overline{s}\left(z_\xi^{'}\cos\theta\sin\alpha-\cos\alpha\right)+\left[1+\left(z_\xi^{'}\right)^2\right]^{1/2}C_{1m2}\right)}$$

$$-P\left[1+\left(z_\xi^{'}\right)^2\right]^{-1/2}\left(\cos\theta\sin\alpha+z_\xi^{'}\cos\alpha\right)\left(z_\xi^{'}\cos\theta\sin\alpha-\cos\alpha\right)$$

(27)

It is assumed that $\rho(R,\ \theta)=0$ for $\theta\in[-\pi/2,\ \pi/2]$ by referring to Fig. 1(b). The following equation determining the boundary condition for the radial stress can thus be obtained by substituting $\rho(R,\ \theta)=0$ for $\theta\in[-\pi/2,\ \pi/2]$ into the expression for ρ in the preceding equation so that

$$\sigma_\xi\left(\xi,\theta\right)\Big|_{\substack{\xi=R,\\ \theta\in[-\pi/2,\pi/2]}}=\left(1+4a^2R^2\right)\omega^2R^2\tau+P\left(2a\right)^{-1}\left(1+4a^2R^2\right)$$
$$\left(2aR\cos\theta\sin\alpha-\cos\alpha\right)\left[\left(1+4a^2R^2\right)^{-1/2}\left(2aR\cos\theta\sin\alpha-\cos\alpha\right)+C_{c2}\right]\Big|_{\theta\in[-\pi/2,\pi/2]}$$

(28)

The preceding equation is taken as the boundary condition for the first-order PDE governing the radial stress. It is clear that an analytical solution will be preferred if available for the problem, if the expression for the required reflectivity profile can be obtained in explicit analytical form. Numerical solutions are poor at providing a deep understanding of the required reflectivity profiles. However, complicated nonlinearities arise with the non-perfect SRP model, besides the ideal model also considered in this paper. Therefore, it is not possible to obtain analytical solutions

because of this nonlinearity when using the non-perfect SRP model. Instead numerical solutions are used to solve the inverse problem. The reflectivity profile $\rho(\xi, \theta)$ can be obtained by substituting the numerical integration based $\sigma_\xi(\xi, \theta)$ profile into the $\rho(\xi, \theta)$ governing equation.

Therefore, the ideal SRP force model will now be used and the required analysis performed and so comparisons will be made between the two models. The governing PDEs for the ideal SRP model can be obtained as follows.

$$\begin{aligned}
&\frac{\partial \sigma_\xi}{\partial \xi} - \sigma_\xi z_\xi^{'} z_\xi^{''} \left[1+\left(z_\xi^{'}\right)^2\right]^{-1} + \omega^2 \xi \tau \left[1+\left(z_\xi^{'}\right)^2\right] \\
&+ P z_\xi^{'} \left[1+\left(z_\xi^{'}\right)^2\right]^{1/2} \cos^2\psi + \rho P z_\xi^{'} \left[1+\left(z_\xi^{'}\right)^2\right]^{1/2} \cos^2\psi = 0 \\
&\frac{\partial \sigma_\eta}{\partial \theta} = 0 \\
&\frac{\partial \sigma_\xi}{\partial \xi} z_\xi^{'} + \sigma_\xi z_\xi^{''} - \sigma_\xi \left(z_\xi^{'}\right)^2 z_\xi^{''} \left[1+\left(z_\xi^{'}\right)^2\right]^{-1} \\
&- P\cos^2\psi \left[1+\left(z_\xi^{'}\right)^2\right]^{1/2} - \rho P \cos^2\psi \left[1+\left(z_\xi^{'}\right)^2\right]^{1/2} = 0
\end{aligned} \tag{29}$$

It is concluded that σ_η is independent of θ and σ_η will be non-negative if $\sigma_\eta \geq 0$ for $\theta=0$. By taking $\partial\sigma_\xi/\partial\xi$ and ρ as the unknowns, one can obtain the following equations.

$$\begin{aligned}
&\frac{\partial \sigma_\xi}{\partial \xi} = -\omega^2 \tau \xi \\
&\rho = \frac{\sigma_\xi z_\xi^{''} \left[1+\left(z_\xi^{'}\right)^2\right]^{-1/2}}{P\left(z_\xi^{'}\cos\theta\sin\alpha - \cos\alpha\right)^2} - \frac{\omega^2 \xi \tau z_\xi^{'} \left[1+\left(z_\xi^{'}\right)^2\right]^{1/2}}{P\left(z_\xi^{'}\cos\theta\sin\alpha - \cos\alpha\right)^2} - 1
\end{aligned} \tag{30}$$

It can be seen that the differential equation governing radial stress in Eq. (30) coincides with Eq. (4.2b) in [11]. The differential equation corresponding to Eq. (4.2a) in [11] is not presented as the transverse elastic deformation is known for the formulated inverse problem. One can also conclude that the expression for ρ in Eq. (30) agrees with Eq. (4.3) in [11] when $\alpha=\pi$ in Eq. (30). One should note that τ denotes the areal density and volume density in this paper and [11] respectively. From the first equation, one has

$$\sigma_\xi = -\frac{1}{2}\omega^2 \xi^2 \tau + \sigma_0 \tag{31}$$

It is evident that σ_0 is independent of ξ but depends on θ, α etc. It is also assumed that $\rho(R, \theta)=0$ for $\theta \in [-\pi/2, \pi/2]$, as for the non-perfect SRP force model. Therefore, one has

$$\sigma_\xi\left(R,\theta\right)\Big|_{\theta\in[-\pi/2,\pi/2]} = \frac{P\left(2aR\cos\theta\sin\alpha - \cos\alpha\right)^2}{2a\left(1+4a^2R^2\right)^{-1/2}} + \omega^2 R^2 \tau\left(1+4a^2R^2\right) \tag{32}$$

where $\sigma_\xi(R, \theta)|_{\theta\in[-\pi/2, \pi/2]}$ is the stress for $\theta \in [-\pi/2, \pi/2]$ at the edge of the reflector. This is taken as the boundary condition when solving the coupled differential-algebraic equations as presented in Eq. (30).Generally speaking, m boundary conditions are required for solving m-order differential equations. Again it can be seen that $\sigma_\xi(R, \theta)|_{\theta\in[-\pi/2, \pi/2]}$ depends on α and ω etc. One can arrive at the expression for σ_0 as follows by substituting the preceding equation into the expression for σ_ξ so that.

$$\sigma_0 = \frac{1}{2}\omega^2 R^2 \tau + \omega^2 R^2 \tau \left(1 + 4a^2 R^2\right) + P(2a)^{-1}\left(1 + 4a^2 R^2\right)^{1/2}\left(2aR\cos\theta\sin\alpha - \cos\alpha\right)^2 \tag{33}$$

It can be seen that σ_0 depends on α and θ for a reflector with constant R, τ, a and ω. Because of the symmetry of the reflector about Oxz, $\sigma_0(\theta) = \sigma_0(-\theta)$ holds in Eq. (33). Since σ_0 is obtained as given in Eq. (33), the complete solution to $\sigma_\xi(\xi, \theta)$ is expressed as follows by substituting Eq. (33) into Eq. (31).

$$\sigma_\xi = -\frac{1}{2}\omega^2 \xi^2 \tau + \frac{1}{2}\omega^2 R^2 \tau + \omega^2 R^2 \tau \left(1 + 4a^2 R^2\right) + P(2a)^{-1}\left(1 + 4a^2 R^2\right)^{1/2}\left(2aR\cos\theta\sin\alpha - \cos\alpha\right)^2 \tag{34}$$

It can be seen that for a reflector with a non-zero spin rate, one can find the largest $\sigma_\xi(\xi, \theta)$ at ξ=0. For a non-spinning reflector, $\sigma_\xi(\xi, \theta)$ is independent of ξ. Moreover, $\sigma_\xi(\xi, \theta)$ is positive throughout the reflector as the summation of the first two terms are positive everywhere. The reflectivity for the ideal SRP force model can thus be obtained by substituting the preceding expression for σ_ξ into Eq. (30).

It is not enough to ensure that $\sigma_\xi \geq 0$ and $\rho \in [0, \rho_{max}]$ because σ_η should also be non-negative, consistent with the fact that the membrane can never withstand compression loads.

The circumferential stress equations for the non-perfect (Eq. (26)) and ideal (Eq. (29)) SRP force models can be found in the preceding section. For the two cases, one tries to demonstrate that σ_η is non-negative and meanwhile that its magnitude is not large when the surface of the solar reflector is controlled to be a paraboloid. It is simple to conclude that σ_η will be non-negative across the reflector as long as $\sigma_\eta(\xi, 0)$ is non-negative. To demonstrate this conclusion, one selects a symmetrical (about the Ox axis) infinitesimal element at any radial position as shown in Fig. 3.

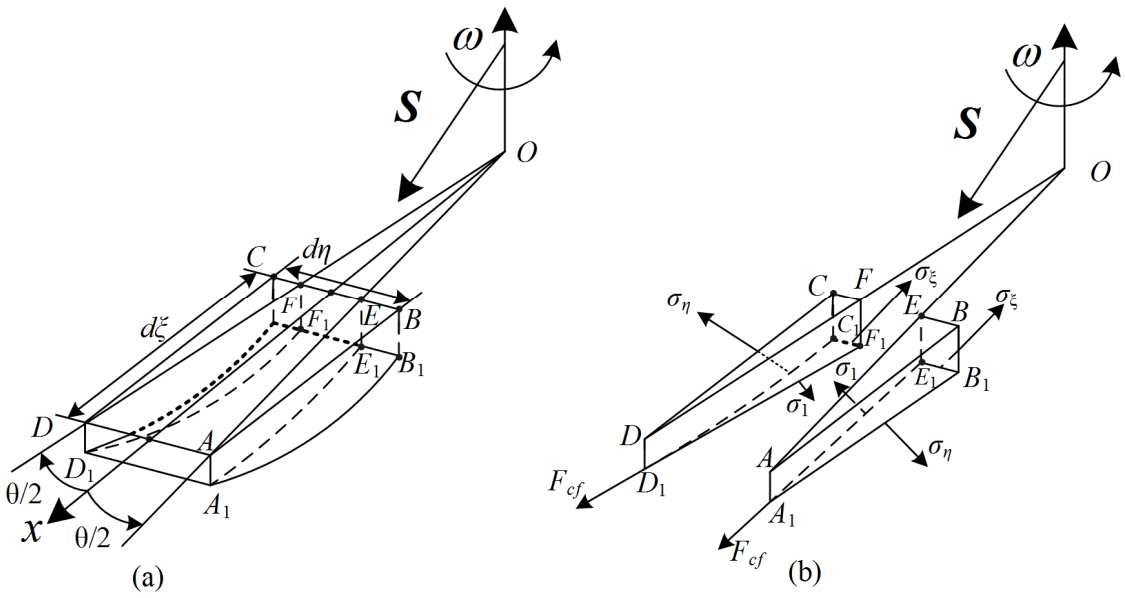

Fig. 3. An arbitrary infinitesimal element used for determining the circumferential stress within the paraboloid reflector

In Fig. 3, $A_1B_1C_1D_1$ is a part/section of the paraboloid, and $ABCD$ is the corresponding projected rectangle on to the hoop plane. One connects O to D and O to A respectively. The angles

between OA and x, OD and x are $\theta/2$. The intersecting points between OA and BC, OD and BC are E and F respectively. E_1E and F_1F are both perpendicular to $ABCD$, E_1 and F_1 are on B_1C_1. One should demonstrate that $\sigma_\eta \geq 0$ when θ approaches 0 as shown in Fig. 3. One can analyze the equilibrium equation along the Ox direction for $D_1F_1C_1$ and/or $A_1E_1B_1$ experiencing the SRP force, centripetal force, and the internal stresses to demonstrate that $\sigma_\eta(\xi, 0) \geq 0$.

The internal tensions along the Ox direction for F_1C_1 and F_1D_1 are calculated as follows.

$$\begin{aligned} T_{\xi\xi} &= -\sigma_\xi \left[1+\left(z_\xi'\right)^2\right]^{-1/2} \tan\left(\theta/2\right) d\xi \sim O\left(\varepsilon^2\right) \\ T_{1\xi} &= \sigma_1 \sqrt{1+\left(z_\xi'\right)^2}\, d\xi \sec\left(\theta/2\right) \sin\left(\theta/2\right) \sim O\left(\varepsilon^2\right) \end{aligned} \tag{35}$$

where ε is a first-order small quantity and $\xi \sim O(\varepsilon)$. The centripetal force experienced by $D_1F_1C_1$ along the Ox direction is then given by

$$F_{cf} = \xi \sec\left(\theta/2\right) \omega^2 \tau \cdot \frac{1}{2} d\xi \tan\left(\theta/2\right) d\xi \sqrt{1+\left(z_\xi'\right)^2} \cos\left(\theta/2\right) \sim O\left(\varepsilon^3\right) \tag{36}$$

The SRP load along the Ox direction can then be calculated as follows.

$$\begin{aligned} F_{n\xi} &= \left[P z_\xi' \cos\psi \left(\cos\psi + C_{c2}\right) d\xi \tan\left(\theta/2\right) d\xi \right. \\ &\quad \left. + \rho z_\xi' \left(\overline{s}\cos\psi + C_{1m2}\right) P \cos\psi d\xi \tan\left(\theta/2\right) d\xi \right] \cos\left(\theta/2\right) \sim O\left(\varepsilon^3\right) \\ F_{t\xi} &= \left\{ P f_{t\xi} \cos\psi \left[1+\left(z_\xi'\right)^2\right]^{-1/2} d\xi \tan\left(\theta/2\right) d\xi \right. \\ &\quad \left. - \rho \overline{s} P f_{t\xi} \cos\psi \left[1+\left(z_\xi'\right)^2\right]^{-1/2} d\xi \tan\left(\theta/2\right) d\xi \right\} \cos\left(\theta/2\right) \sim O\left(\varepsilon^3\right) \end{aligned} \tag{37}$$

The following equilibrium condition along the Ox direction can thus be established for $D_1F_1C_1$ as

$$T_{\xi\xi} + T_{1\xi} + F_{n\xi} + F_{t\xi} + F_{cf} = 0 \tag{38}$$

In Eq. (38), the equilibrium equation is established by considering the internal tensions ($T_{\xi\xi}$ and $T_{1\xi}$), centripetal force (F_{cf}) and SRP loads ($F_{n\xi}$, and $F_{t\xi}$) within $D_1F_1C_1$. One can then arrive at the expression for σ_1 as follows by substituting Eqs. (35-37) into Eq. (38).

$$\begin{aligned} \sigma_1 &= \sigma_\xi \left[1+\left(z_\xi'\right)^2\right]^{-1} - \xi \sec\left(\theta/2\right) \omega^2 \tau \cdot \left(d\xi/2\right) \\ &\quad - \left(1-\rho\overline{s}\right) P f_{t\xi} \cos\psi \left[1+\left(z_\xi'\right)^2\right]^{-1} d\xi \\ &\quad - P z_\xi' \left[1+\left(z_\xi'\right)^2\right]^{-1/2} \cos\psi \left(\cos\psi + C_{c2}\right) d\xi \\ &\quad - \rho z_\xi' \left[1+\left(z_\xi'\right)^2\right]^{-1/2} \left(\overline{s}\cos\psi + C_{1m2}\right) P \cos\psi d\xi \sim O\left(\sigma_\xi\right) > 0 \end{aligned} \tag{39}$$

A conclusion is that σ_1 is smaller than σ_ξ, besides $\sigma_1 \sim O(\sigma_\xi) > 0$ in the preceding equation. In fact, this conclusion coincides with the observation that the solar reflector will mainly experience radial tension, as expected. Similarly, one can also find that $\sigma_\eta \sim O(\sigma_\xi, \sigma_1) > 0$ by establishing the equilibrium equation along the Oy direction. Moreover, σ_η is also smaller than σ_ξ. In fact, it is clear that the above-mentioned conclusions are not only effective for $\theta=0$, but are also valid for any other positions within the reflector. Thus, it is verified and concluded that the circumferential

stress is non-negative and is of the same order as the radial stress, but smaller than the radial stress.

4. Results and discussions

The hoop radius R and the focal length of the paraboloid f are two key parameters to evaluate the performance of the reflector. The latter is especially important as some key functions of the reflector are determined by f. The latter is defined as [11]

$$f = \frac{R^2}{4|d|} = \frac{R^2}{4|aR^2|} = \frac{1}{4a} \tag{40}$$

The parameters R, a and d in the preceding equation can be found in Eqs. (21-22). Generally, one hopes that f should be as small as possible to make the performance of the reflector better. However, unfortunately it will be seen later that one will fail to generate a paraboloid form if f is too small with a constant fixed R. One may also hope that R should be as large as possible when f is fixed. However, one will also find that a reflector with a large radius is also difficult to generate in a paraboloid. Besides R and f (S or k), surface shape control will also be influenced by ω and the SRP force model. One can see that there exists two independent parameters for a paraboloid reflector by analyzing Eq. (21). One can select any two parameters among R, f, S, and k as two independent parameters to determine a paraboloid as introduced previously. The first two parameters are selected as they are the most suitable to evaluate the performance of the reflector.

As noted previously, the radial and circumferential stresses should not be negative since the membrane can never experience compressive loads, nor should they be large because the reflector material can withstand limited stresses. Intuitively, one can predict that the maximal stress the reflector experiences can hardly reach its material limit since the SRP and centripetal forces experienced will likely be small. In this paper, we only check the order of the magnitude of the radial stress since the smaller circumferential stress has the same order of magnitude at most. Besides the stress, one should focus on the reflectivity profile across the reflector and ensure that ρ at any position within the reflector is within the practical range [0, 0.88].

In this section, the analysis and discussion will be performed based on the ideal and non-perfect SRP force models respectively. The analytical solution for the ideal SRP force model has already been presented in the preceding section. For the non-perfect SRP force model, it is difficult or impossible to obtain analytical solutions because of the nonlinearity, as explained previously, and so a numerical integration scheme is utilized.

Before performing numerical analysis for various case studies, the verification of the analysis method and results presented in this paper will be clarified. The reliability of the method and results can be supported by comparing the reflectivity profiles of the simplified cases in this paper with the corresponding profiles in [11]. The case with $\alpha=\pi$ and $\omega=0$ is considered and the ideal SRP force model is used. The results as presented in Fig. 10 in [11] will be taken as the benchmarks. The required reflectivity profiles for S=101 m - 106 m will be calculated using the approach in this paper with S indicating the slack length of the reflector. One can note that the projection of S onto the hoop plane is the reflector diameter [11]. Figure 4 shows the reflectivity profiles in this paper and the corresponding profiles in Fig. 10 in [11].

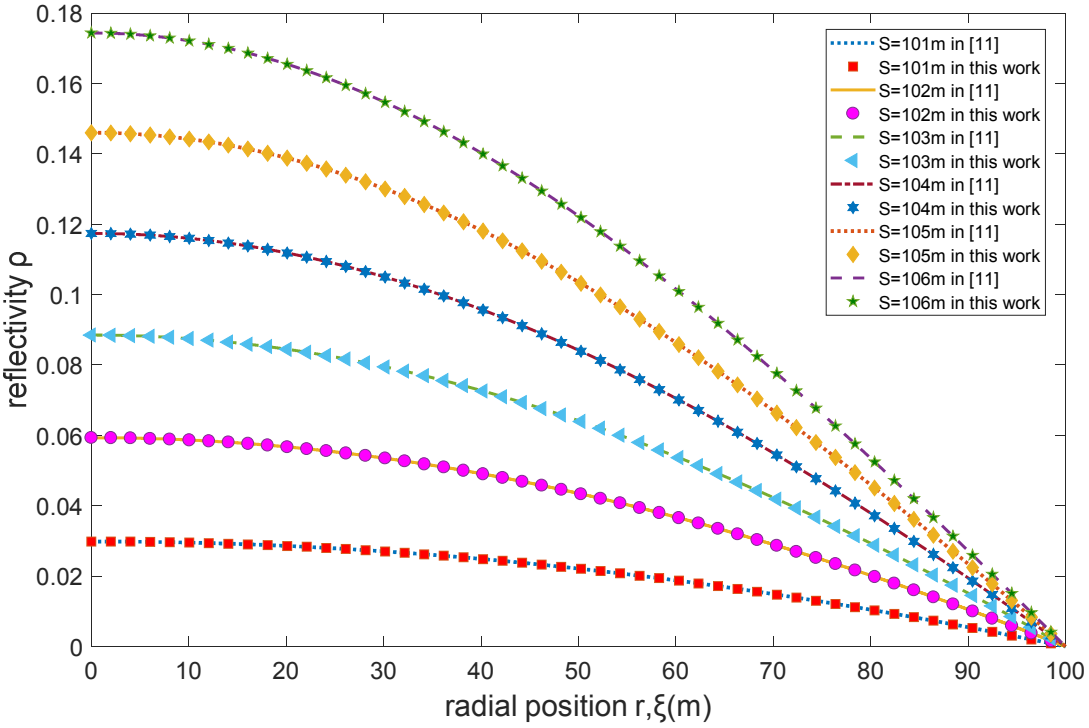

Fig. 4. Reflectivity profiles taken from Ref. [11] and the corresponding results in this paper

It is evident that the required reflectivity profiles in this paper coincide with the corresponding profiles in [11] when the same parameters are used. This provides confidence in the analysis method used.

For a solar reflector with an invariant fixed radius (R=100 m) and membrane area (k=1.05, i.e., f=110 m), we will study the results influenced by the angular velocity ω and the tilt angle α. Firstly, a non-spinning (ω=0) reflector with a tilt angle α=0.1π *rad* is considered, and the results are presented in Figs. 5-6 and Figs. 7-8 for the reflector with an ideal and non-perfect SRP force models respectively. The density of the reflector is 3.93×10^3 kg/m^3 and the thickness is 2.5 μm throughout the paper. The areal density τ is therefore 0.009825 kg/m^2.

The analytical analysis will be performed for the ideal SRP force model first. For the radial stress (Eq. (32)), the derivative of σ_ξ with respect to θ is as follows for ω=0.

$$\frac{\partial \sigma_\xi}{\partial \theta} = -2PR\sin\alpha\left(1+4a^2R^2\right)^{1/2}\left(2aR\cos\theta\sin\alpha-\cos\alpha\right)\sin\theta \tag{41}$$

For the paraboloid solar reflector whose surface shape is controlled by the SRP force, it is concluded that cosψ in Eq. (8) is always positive at any position within the reflector, which means merely that the front side of the reflector experiences the SRP force, equivalently expressed as $\dot{z}_\xi\cos\theta\sin\alpha-\cos\alpha>0$ for any θ, ξ, and α. Therefore, it is concluded that $\partial\sigma_\xi/\partial\theta<0$ for $\theta\in[0, \pi/2]$. Due to the symmetry of the problem, it is concluded that the largest and smallest σ_ξ can be presented as follows

$$\begin{aligned}
\sigma_{\xi l}\big|_{\theta=0} &= P(2a)^{-1}\left(1+4a^2R^2\right)^{1/2}\left(2aR\sin\alpha-\cos\alpha\right)^2 \\
\sigma_{\xi s}\big|_{\theta=\pm\pi/2} &= P(2a)^{-1}\left(1+4a^2R^2\right)^{1/2}\cos^2\alpha
\end{aligned} \tag{42}$$

where the subscripts "*l*, *s*" represent the largest and smallest magnitudes respectively. One can obtain the specific values for $\sigma_{\xi l}|_{\theta=0}$ and $\sigma_{\xi s}|_{\theta=\pm\pi/2}$ once a, R and α are given. One can also see that $\sigma_{\xi}>0$ within the reflector and thus $\sigma_{\eta}>0$ anywhere. From Eq. (30), one can obtain the expression for ρ as

$$\rho=\frac{\sigma_{\xi}z_{\xi}^{''}\left[1+\left(z_{\xi}^{'}\right)^{2}\right]^{-1/2}}{P\left(z_{\xi}^{'}\cos\theta\sin\alpha-\cos\alpha\right)^{2}}-1 \tag{43}$$

The partial derivative of ρ with respect to θ is as follows.

$$\frac{\partial\rho}{\partial\theta}\Big/4\sqrt{4a^{2}R^{2}+1}=\left[\frac{\left(2aR\cos\theta\sin\alpha-\cos\alpha\right)^{2}a\xi\sin\theta\sin\alpha}{\sqrt{4a^{2}\xi^{2}+1}\left(2a\xi\cos\theta\sin\alpha-\cos\alpha\right)^{3}}-\frac{\left(2aR\cos\theta\sin\alpha-\cos\alpha\right)aR\sin\theta\sin\alpha}{\sqrt{4a^{2}\xi^{2}+1}\left(2a\xi\cos\theta\sin\alpha-\cos\alpha\right)^{2}}\right]\le 0\Big|_{\theta\in[0,\pi/2]} \tag{44}$$

It is concluded that ρ reaches its largest magnitude for θ=0. Next, substituting θ=0 into the expression for ρ, and calculating its derivative with respect to ξ, one has

$$\frac{\partial\rho}{\partial\xi}\Big/4\sqrt{4a^{2}R^{2}+1}=-\left[\frac{\left(2aR\sin\alpha-\cos\alpha\right)^{2}a^{2}\xi}{\left(4a^{2}\xi^{2}+1\right)^{3/2}\left(2a\xi\sin\alpha-\cos\alpha\right)^{2}}+\frac{\left(2aR\sin\alpha-\cos\alpha\right)^{2}a\sin\alpha}{\left(4a^{2}\xi^{2}+1\right)^{1/2}\left(2a\xi\sin\alpha-\cos\alpha\right)^{3}}\right]\le 0 \tag{45}$$

Therefore, it is concluded that ρ reaches its largest magnitude when θ=0 *rad* and ξ=-100 m. The consistency between these analytical results and the numerical results can be seen in Figs. 5-6. The stress and reflectivity profiles are calculated relative to *Oxyz* where $\theta\in[-\pi/2, \pi/2]$ is adopted and therefore $\xi\in$[-100, 100] should be adopted to cover all positions within the solar reflector. One can see the details of the reference frames and reflector configuration in Fig. 1.

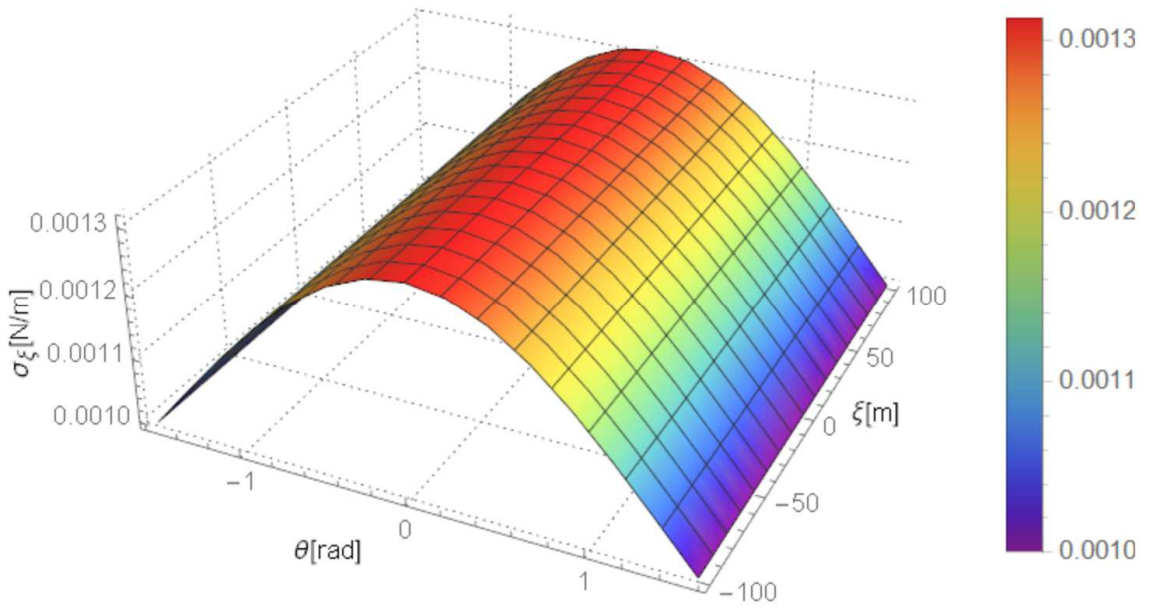

Fig. 5. Normal stress $\sigma_\xi(\theta, \xi)$ for the ideal SRP force model

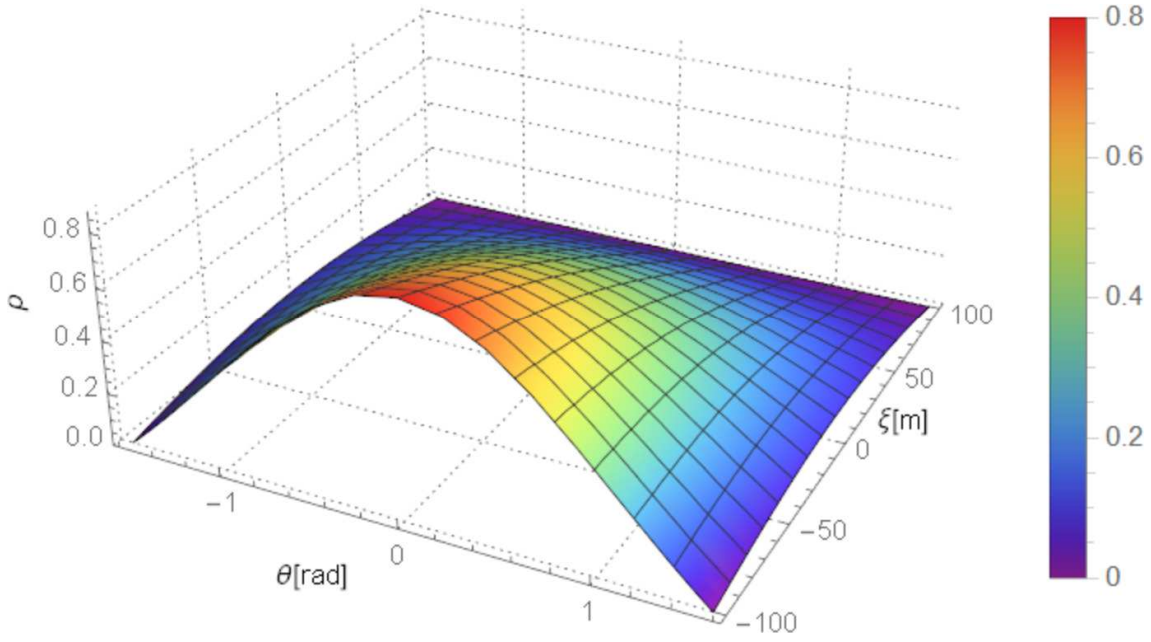

Fig. 6. Required reflectivity profile $\rho(\theta, \xi)$ for the ideal SRP force model

From Fig. 5, it can be seen that $\sigma_\xi(\theta, \xi)$ reaches its largest and smallest magnitudes when θ=0 and $\pm\pi/2$ respectively. One can find that $\sigma_{\xi l}\approx 0.00131$ *N*/*m* and $\sigma_{\xi s}\approx 0.001$ *N*/*m* either analytically or numerically, the stress level (approximately 10^3Pa) is therefore far from the typical material strength limitation level (of order 10^8Pa) [24]. Moreover, the order of the elastic strain is approximately 10^{-6} and is thus negligible. The strength of the materials available for the reflector can therefore withstand the loads in this case. Theoretically, the solar reflector can be controlled to be a paraboloid as the normal and circumferential stresses, together with the reflectivity, are within feasible ranges as presented and discussed.

However, the aforementioned conclusions presented for the ideal SRP force model are not valid for the non-perfect SRP model. The stress and reflectivity for the reflector with the

non-perfect SRP force model are presented in Figs. 7-8 using the same parameters as used for the reflector with the ideal SRP force model previously.

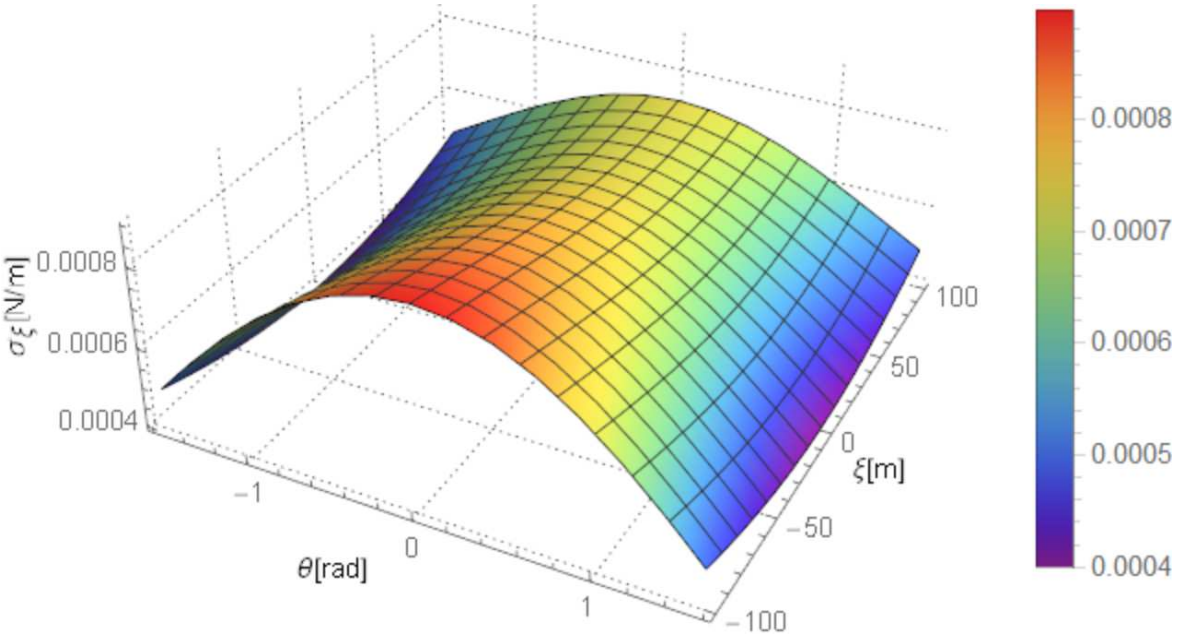

Fig. 7. Normal stress $\sigma_\xi(\theta, \xi)$ for the non-perfect SRP force model

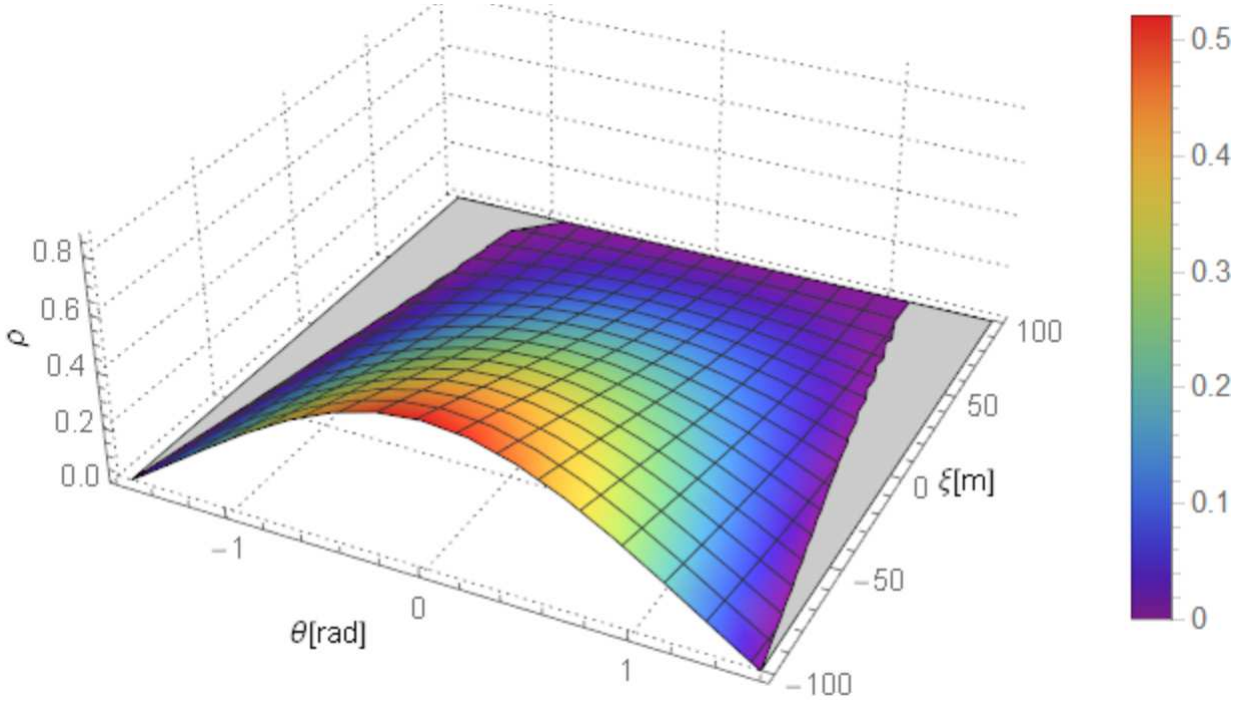

Fig. 8. Required reflectivity profile $\rho(\theta, \xi)$ for the non-perfect SRP force model

One can see that although σ_ξ and σ_η are within the feasible range (positive and not large), the required reflectivity $\rho(\theta, \xi)$, however, is within an unrealistic range since $\rho(\theta, \xi)$ is negative in the grey region as shown in Fig. 8. This is clearly physically unrealizable and is due to the complexity of the non-perfect SRP force model. However, one can correct issue this by rotating the reflector.

One can try to merely rotate the reflector without changing α, R and k for the reflector with the non-perfect SRP model to control the surface shape using reasonable inputs (that is $\rho(\theta, \xi) \in [0,$

0.88]) and meanwhile with reasonable (positive and not over-large) stresses generated. It is found that the reflector can be controlled to be a paraboloid successfully when $\omega \in [0.065, 0.2018]$ deg/s. The stresses and the reflectivity profiles are presented in Fig. 9 (when ω=0.2018 deg/s) and Fig. 10 (when ω=0.0650 deg/s) respectively. It should be noted that the reflectivity and stress profiles change with time when the reflector rotates as all results are calculated relative to *Oxyz*.

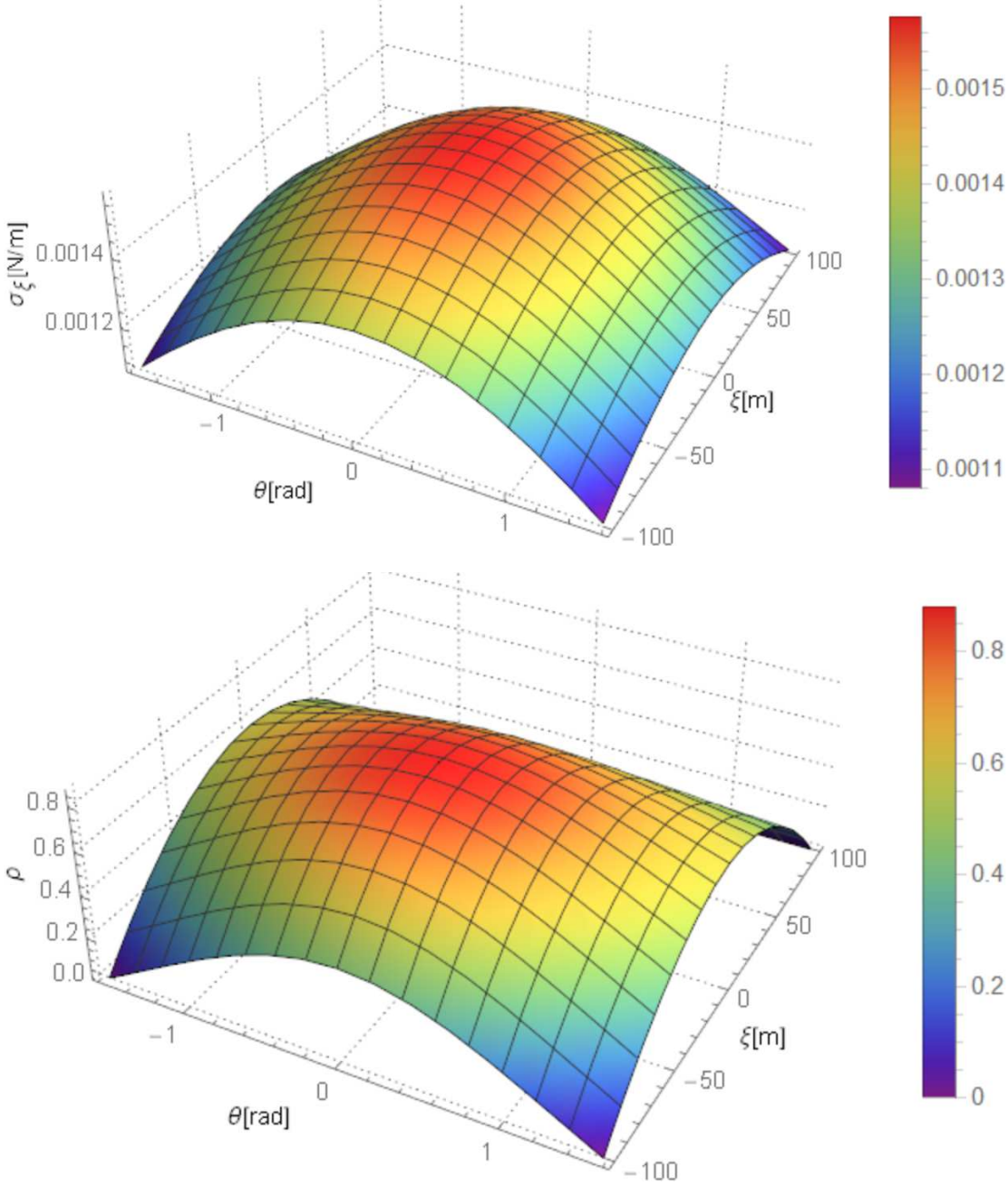

Fig. 9. The normal stress $\sigma_\xi(\theta, \xi)$, the required reflectivity profile $\rho(\theta, \xi)$ when ω=0.2018 deg/s

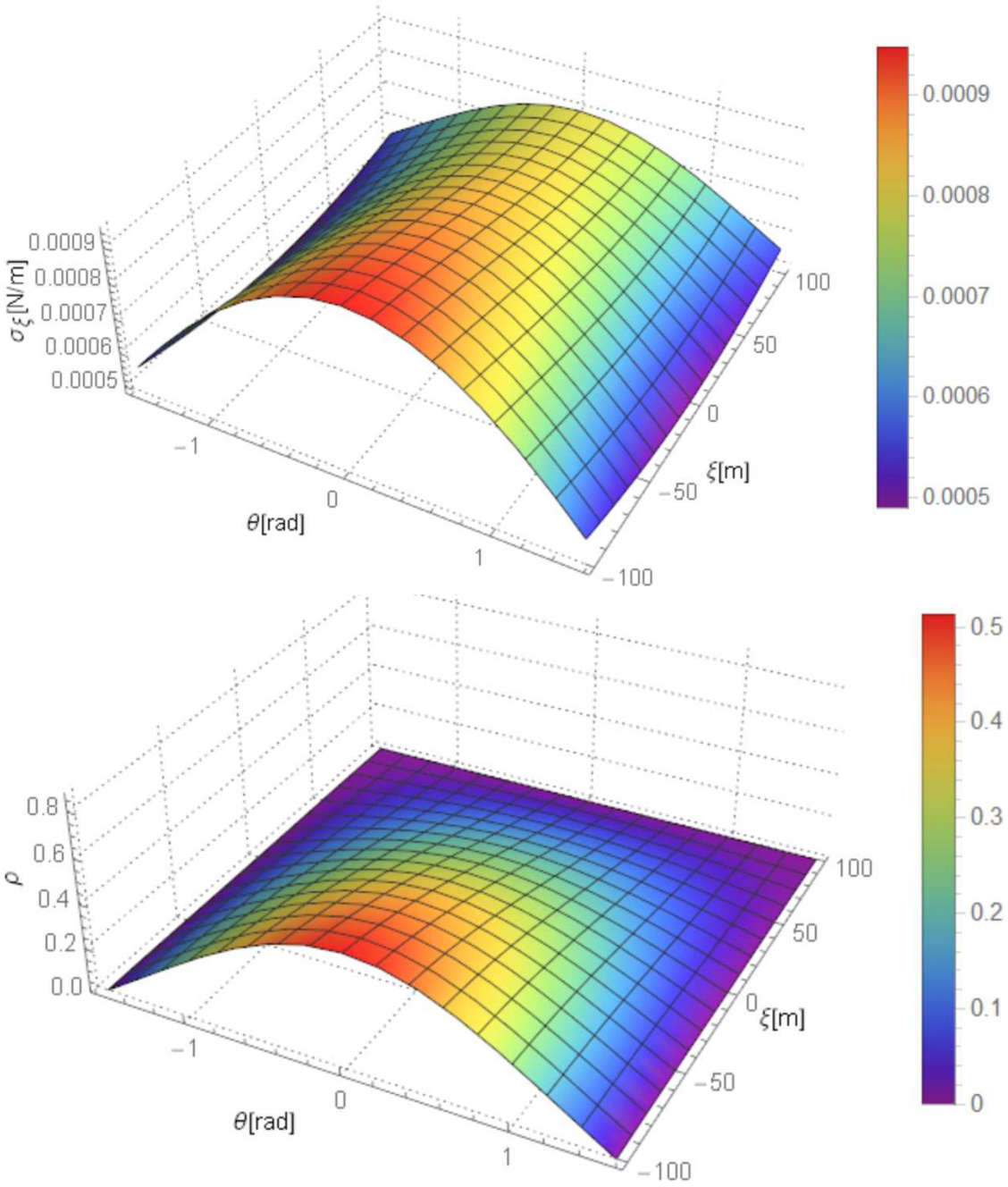

Fig. 10. The normal stress $\sigma_\xi(\theta, \xi)$, the required reflectivity profile $\rho(\theta, \xi)$ when ω=0.065 deg/s

It is interesting to note that one can correct the surface shape not only by modulating the SRP force across the reflector but also by rotating the reflector, which is usually required for a large flexible reflector to provide rigidity, such as the IKAROS solar sail. As stated in [11], the effect of the centripetal force is to push the reflector film material away from the spin axis and can compensate for the required upward SRP force in Fig. 8, which requires the reflectivity to be negative. The effectiveness of rotating the reflector is verified and the feasible region is also presented. It can be seen that one should increase ω from 0 to 0.0650 deg/s at least to make $\rho(\theta, \xi)$ non-negative everywhere, and from 0.0650 to 0.2018 deg/s to make $\rho(\theta, \xi) \in [0, 0.88]$ everywhere. The stress level is relatively low for all feasible ω, within the strength limitation of available reflector materials.

If one relaxes the constraint ω=0, and takes both ω and α as varying parameters for the

reflector with R=100 m and k=1.05, the feasible regions of ω and α are given for the two SRP models as shown in Fig. 11.

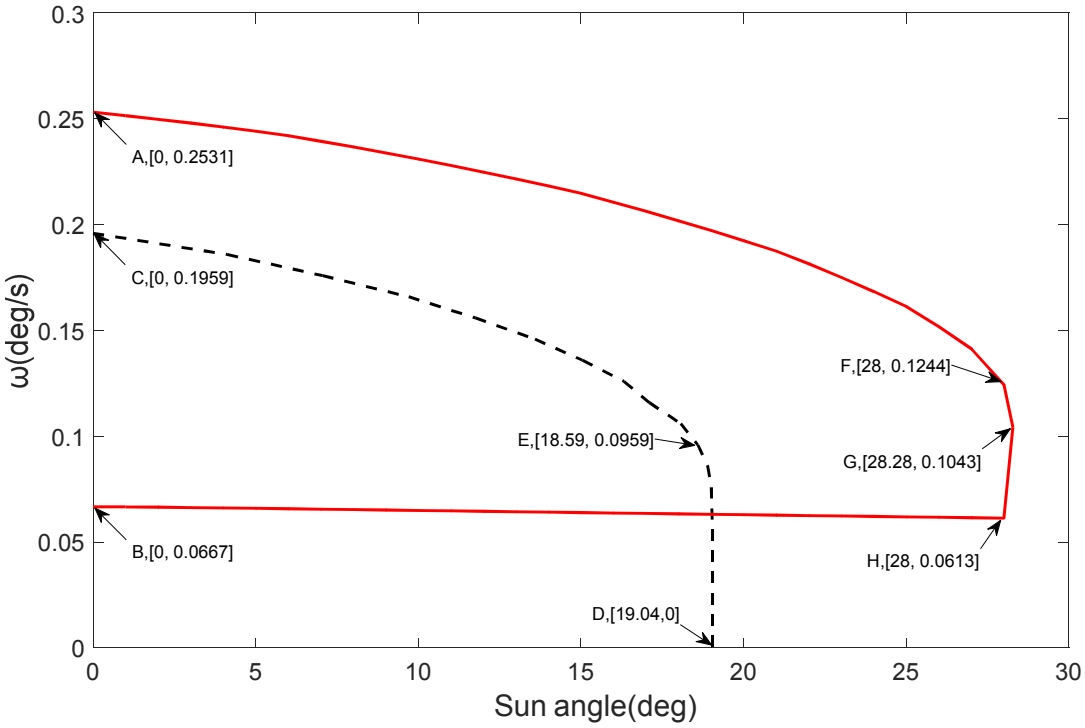

Fig. 11. Feasible regions of ω and (π-α) for the two SRP models when R=100, k=1.05 (f=110 m), the dotted and solid lines indicate the feasible boundaries for the ideal and non-perfect SRP models respectively

In Fig. 11, the Sun angle is (π-α) where one can find α in Fig. 1(b). The boundaries of the feasible regions for the ideal and non-perfect SRP models consist of the dotted line and the two axes, the solid line and the vertical axis respectively, as shown in Fig. 11. It can be seen that the feasible regions between the two models are different. As noted previously in Figs. 8-10 (a special case corresponding to α=0.1π rad), the reflector can never be a paraboloid if $\omega<\omega_l$ (ω_l is the angular velocity at the lower boundary) or $\omega>\omega_h$ (ω_h is the angular velocity at the upper boundary) when the non-perfect SRP force model is used. Moreover, ρ will be negative in parts of the reflector when $\omega<\omega_l$, and will be larger than 0.88 when $\omega>\omega_h$. In conclusion, the smallest ρ is zero on curve BH, the largest ρ is 0.88 on curve $AFGH$. For the ideal SRP model, ρ will be never negative. The sensitiveness of the boundaries (not including the axes) of the feasible regions to variations of the Sun angle can also be observed. The variations of the boundaries are not affected dramatically by the variation of the Sun angle for curve AF, BH and CE, however, they change dramatically for curve FH and DE. It is therefore recommended that ω and α should be far from the boundary.

One may be interested in the magnitude of the largest stress within the reflector after analyzing the reflectivity profile. To analyze the stress within the reflector for the ideal SRP model, one can obtain $\partial\sigma_\xi/\partial X$ ($X=\theta$, ξ) as follows.

$$\begin{aligned}\frac{\partial\sigma_\xi}{\partial\xi}&=-\omega^2\xi\tau,\\ \frac{\partial\sigma_\xi}{\partial\theta}&=-2PR\sin\alpha\left(1+4a^2R^2\right)^{1/2}\left(2aR\cos\theta\sin\alpha-\cos\alpha\right)\sin\theta\end{aligned}\tag{46}$$

It is evident that the smallest and largest values for σ_ξ, together with the corresponding positions can be obtained as follows respectively.

$$\begin{aligned}\sigma_{\xi l}\big|_{\substack{\theta=0\\ \xi=0}} &= \frac{1}{2}\omega^2R^2\tau+\omega^2R^2\tau\left(1+4a^2R^2\right)\\ &\quad +P(2a)^{-1}\left(1+4a^2R^2\right)^{1/2}\left(2aR\sin\alpha-\cos\alpha\right)^2\geq 0\\ \sigma_{\xi s}\big|_{\substack{\theta=\pm\pi/2\\ \xi=\pm R}} &= \omega^2R^2\tau\left(1+4a^2R^2\right)+P(2a)^{-1}\left(1+4a^2R^2\right)^{1/2}\cos^2\alpha\geq 0\end{aligned} \tag{47}$$

It can be seen that $\sigma_{\xi s}\geq 0$ when ω and α adopt any values. One can calculate $\partial\sigma_{\xi j}/\partial n$ ($j=l, s$; $n=\omega, \alpha$) and determine the signs as follows.

$$\begin{aligned}&\frac{\partial\sigma_{\xi l}}{\partial\omega}\geq 0,\frac{\partial\sigma_{\xi s}}{\partial\omega}\geq 0,\frac{\partial\sigma_{\xi s}}{\partial\alpha}\leq 0,\frac{\partial\sigma_{\xi l}}{\partial\alpha}=P(a)^{-1}\left(1+4a^2R^2\right)^{1/2}\\ &\cdot\left(2aR\sin\alpha-\cos\alpha\right)\left(2aR\cos\alpha+\sin\alpha\right)\leq 0\big|_{\alpha\in\left[\pi-\frac{19.04}{180}\pi,\pi\right]}\end{aligned} \tag{48}$$

In the preceding expression, the limit 19.04 is obtained from point D in Fig. 11. Therefore, the largest $\sigma_{\xi l}$, which indicates the largest stress at $\xi=0$ and $\theta=0$ when ω and α adopt these values, can be searched for at the dotted boundary in Fig. 11. The largest $\sigma_{\xi l}$ for the non-perfect SRP model can also be searched for within the feasible region. The largest $\sigma_{\xi l}$ for the two SRP models are then shown in Fig. 12.

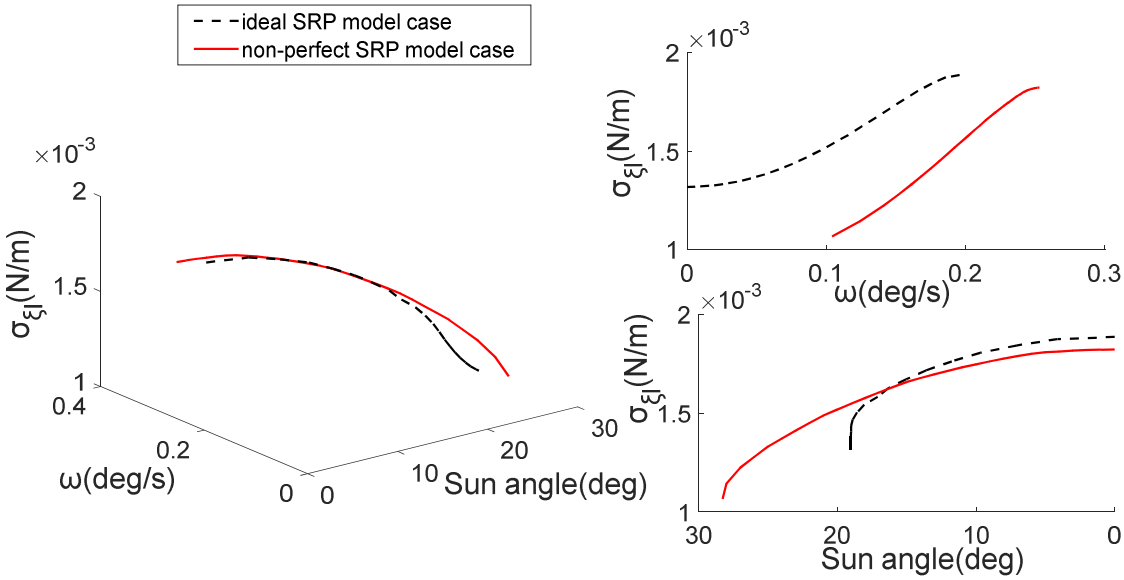

Fig. 12. Largest stress $\sigma_{\xi l}$ as the function of ω and Sun angle when R=100 m, k=1.05

It can be seen that the magnitude of the largest stress is small, of order 10^{-3} N/m (10^3~10^4 Pa). The strength of the typical materials for the reflector membrane can therefore withstand the stress. Besides, it can be seen that the elasticity of the reflector is negligible since the order of magnitude of the elastic strain is merely 10^{-5}~10^{-6} for a reflector with an elastic modulus $E=3.5\times10^9$ N/m^2 [24]. The largest stress is the monotone increasing function of ω and α within the feasible regions. Therefore, one can determine the largest stress for the fixed reflector working within certain conditions ($\omega\in[\omega_l, \omega_h]$, $\alpha\in[\alpha_l, \alpha_h]$).

It is useful for one to study the reflectors operating in specific conditions, e.g., ω=0.45 deg/s and α=145° (Sun angle of 35°). Then R and f will be taken as parameters, with the results presented in Figs. 13-14.

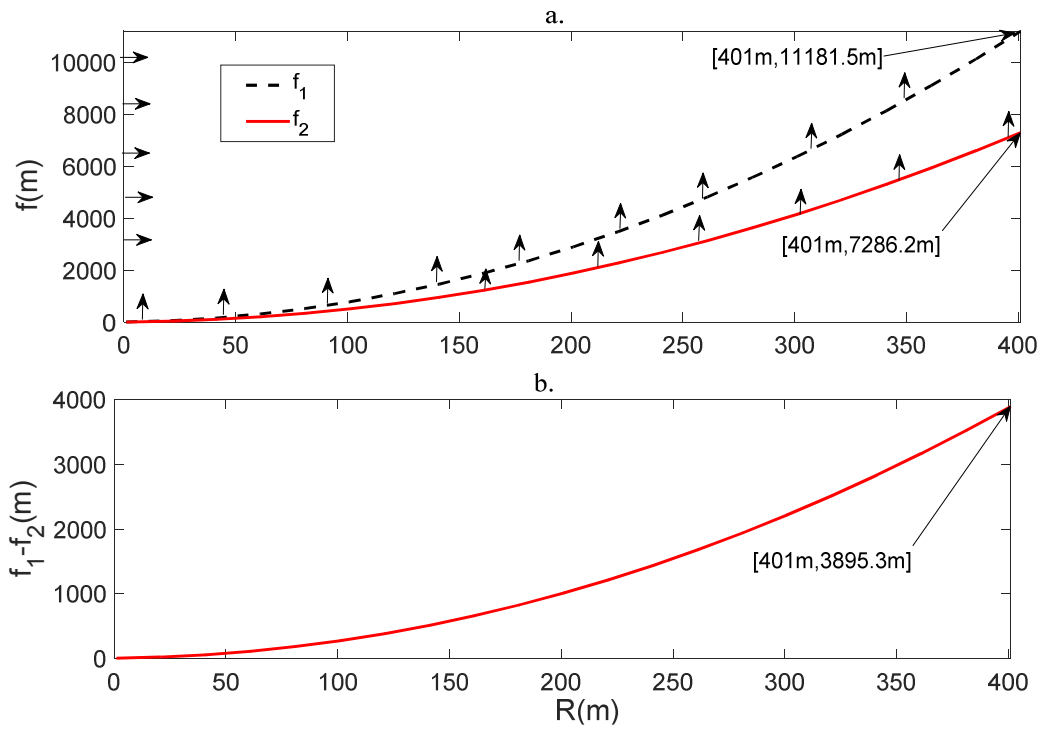

Fig. 13. (a). Feasible regions of f and R for the two SRP models when ω=0.45deg/s and α=145°, the dotted and solid lines indicate the feasible boundaries for the ideal and non-perfect SRP model respectively; (b). focal length difference between the two models

The feasible regions in Fig. 13a for the two models are surrounded by the lines with arrows. The smallest available focal lengths for the ideal and non-perfect SRP force models correspond to the dotted and solid lines respectively. For fixed R, the focal lengths larger than the critical values on the boundary are achievable; similarly, for fixed f, the radius smaller than the critical values on the boundary are achievable. It is interesting to note that the achievable smallest focal length of a reflector with the non-perfect SRP model is smaller than a reflector with the ideal SRP model when adopting the same R. The feasible region for the non-perfect SRP case is larger than that for the ideal SRP case. The difference between the boundaries is presented in Fig. 13b. It can be seen that the difference between the achievable smallest focal length for the two models will increase with R. The largest difference is (11181.5-7286.2) m when R=401 m. The performance of the reflector will be partially determined by the smallest achievable focal length. One can calculate the largest stress within the reflector by restricting the largest focal length, for example to be 12,000 m in Fig. 13a. The largest stress will now be searched for within the region surrounded by f=12,000 m and the feasible region. By simple calculations, it is found that one can merely calculate the largest stress when f=12,000 m and on the solid and dotted boundary lines with arrows in Fig. 13a. The former is given in Fig. 14c and the latter is presented in Fig. 14 a, b and d, where b and d are the views from the R and f directions respectively.

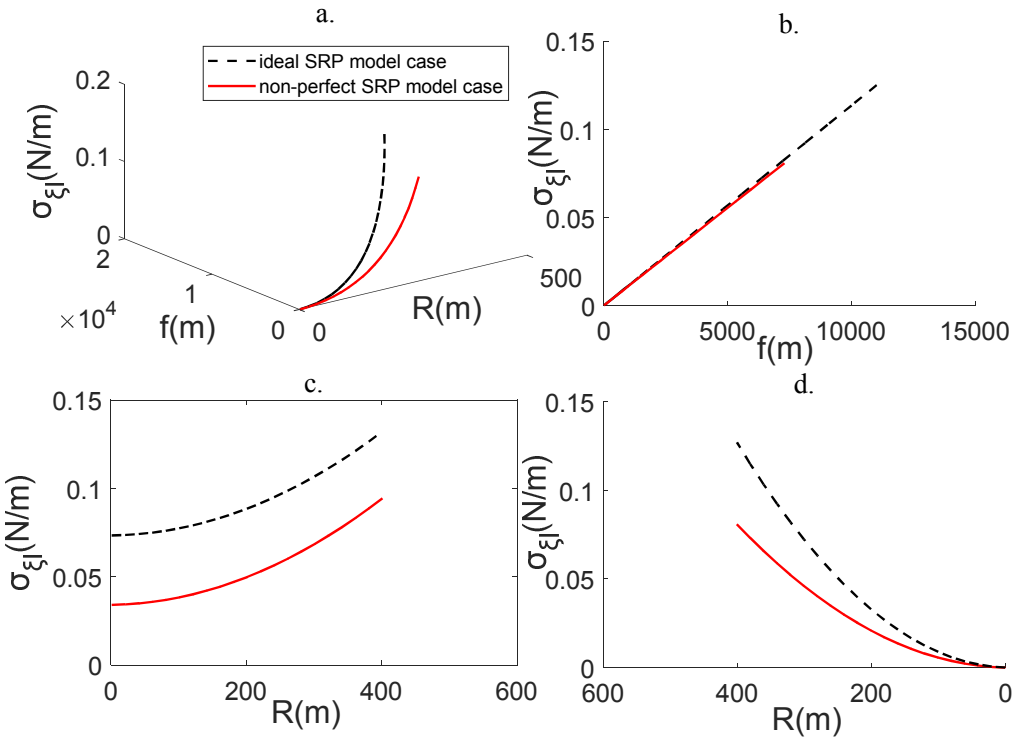

Fig. 14. Largest stress $\sigma_{\xi l}$ as the function of f and R when ω=0.45 *deg*/*s* and α=145°

The stress level reaches approximately 10^{-1} N/m (10^4 Pa~10^5 Pa level) at most. The typical material strength of the reflector is therefore high enough to withstand this small stress. It is clear that the largest stress will increase with R and f, and that the largest stress will be very large when the area coefficient k is extremely small, which is not preferred as one will not design a reflector with an over-large focal length f (i.e., so a small area coefficient k). It is also noted that the elastic strain will be of the order of 10^{-5} for a reflector with an elastic modulus E=3.5×10^9 N/m^2 [24], indicating the elastic deformation is negligible.

5. Conclusions

The paper has focused on modulating the SRP force to control the surface shape of a slack membrane reflector to be a paraboloid. A non-perfect SRP model with realistic membrane parameters and a non-zero Sun angle were considered in the analysis, which have not been considered previously. For a reflector with a constant radius and membrane area (or focal length), the feasible set of spin rates and Sun angles was found where the difference between the ideal and non-perfect SRP models was evident. The lower and upper feasible boundaries for the non-perfect SRP model indicated that the smallest reflectivity ρ is zero and the largest ρ is 0.88 respectively. While for the ideal model, we merely considered the largest reflectivity ρ to be 0.88 for the upper feasible boundary. It is recommended that the parameters of the reflector should be far from these boundaries which were identified. It was also shown that the largest stress level was relatively low (order of 10^3 Pa~10^5 Pa). This small stress makes the deformation of the membrane negligible. The strength of typical membrane materials is enough to support the reflector reliably. We also investigated the reflector working under fixed conditions, that is with an given fixed spin rate and Sun angle. It was shown that the achievable focal length range for the non-perfect SRP model was larger than the corresponding range for the ideal SRP model. Again, it is recommended that one should consider the reflector design with parameters far from the feasible boundaries which were

identified.

6. Acknowledgments

JL was support by NSFC (11302134) and China Scholarship Council program (201508210053). CM was support by a Royal Society Wolfson Research Merit Award.

References

[1] Christopher H.M Jenkins, 2001 "Advanced Concepts", Gossamer Spacecraft: Membrane and Inflatable Structures Technology for Space Applications, Progress in Astronautics and Aeronautics, pp. 553-572. doi.org/10.2514/5.9781600866616.0553.0572

[2] Gong S P, Li J F, Baoyin H. Passive stability design for the solar sail on displaced orbits, Journal of Spacecraft and Rocket, 2007, Vol. 44, No. 5, pp 1071-1080

[3] Imbriale, W.A., Gao, S. & Boccia, L. 2012 Space Antenna Handbook, pp. 466-510, Hoboken: Wiley

[4] MacEwen, H. A. (ed.) 2002 Proceedings of SPIE: Highly innovative space telescope concepts, vol. 4849, 42 papers (426) pages ISBN: 9780819446282

[5] Cougnet, C., Sein, E., Celeste, A. & Summerer, L. 2004 Solar power satellites for space exploration and applications, Proceedings of the 4th International Conference on Solar Power from Space, SPS '04-Together with The 5th International Conference on Wireless Power Transmission, WPT 4849, SPIE-The International Society for Optical Engineering, Bellingham, WA, USA.

[6] McInnes, C. (2017) Harvesting Near Earth Asteroid Resources Using Solar Sail Technology. In: Fourth International Symposium on Solar Sailing (ISSS 2017), Kyoto, Japan, 17-20 Jan 2017.

[7] Freeland, R. E., Bilyeu, G. D., Veal, G. R., Steiner, M. D. & Carson, D. E. 1997 Large inflatable deployable antenna flight experiment results, Acta Astronautica, 41(4-10), pp. 267-277. (doi:10.1016/S0094-5765(98)00057-5)

[8] Siyuan Rong, JiaFu Liu, Biao Zhao, Naigang Cui. Inflatable deployment dynamics simulation of Solar sail spacecraft support tube. 2009 International Conference on Mechatronics and Automation, 2239-2244, 2009

[9] Houfei Fang, Michael Lou, and John Hah. "Deployment Study of a Self-Rigidizable Inflatable Boom", Journal of Spacecraft and Rockets, Vol. 43, No. 1 (2006), pp. 25-30. http://dx.doi.org/10.2514/1.3283

[10] Mori, O., Shirasawa, Y., Mimasu, Y., Tsuda, Y., Sawada, H. et. al. 2014 Overview of IKAROS Mission, Advances in Solar Sailing (ed. M. Macdonald), Springer Praxis Books, Ch. 3, pp. 25-43, Berlin: Springer.

[11] Andreas Borggrafe, Jeannette Heiligers, Matteo Ceriotti, Colin R. McInnes. Shape control of slack space reflectors using modulated solar pressure. Proceedings of the Royal Society A: Mathematical, Physical and Engineering Science, vol. 471, issue 2179, p. 20150119

[12] Shengping Gong, Junfeng Li. Equilibria near asteroids for solar sails with reflection control devices. Astrophys Space Sci (2014) 355:2165 DOI 10.1007/s10509-014-2165-7

[13] Andreas Borggräfe, Jeannette Heiligers, Matteo Ceriotti, Colin McInnes, Optical Control of Solar Sails using Distributed Reflectivity, Spacecraft Structures Conference, AIAA SciTech Forum, (AIAA 2014-0833) http://dx.doi.org/10.2514/6.2014-0833

[14] Ruggiero, E. J. & Inman, D. J. 2006 Gossamer spacecraft: Recent trends in design, analysis, experimentation, and control, Journal of Spacecraft and Rockets, 43(1), pp. 10-24. (doi:10.2514/1.8232)
[15] R. T. HAFTKA and H. M. ADELMAN. An analytical investigation of shape control of large space structures by applied temperatures, AIAA Journal, Vol. 23, No. 3 (1985), pp. 450-457.
[16] C. H. Jenkins, D. K. Marker. Surface Precision of Inflatable Membrane Reflectors. J. Sol. Energy Eng 120(4), 298-305 (Nov 01, 1998) (8 pages)
[17] Haftka, L. M. & Tuan, C. 1987 The formation of optical membrane reflector surfaces using uniform pressure loading, Solar Energy Research Inst., Golden, CO (USA), Rept. SERI/TR-253-3025
[18] Roy D. Kornbluh, David S. Flamm, Harsha Prahlad et al. Shape control of large lightweight mirrors with dielectric elastomer actuation. Proc. SPIE 5051, Smart Structures and Materials 2003: Electroactive Polymer Actuators and Devices (EAPAD), 143 (July 28, 2003); doi:10.1117/12.484405
[19] Gaspar, J., Mann, T., Behun, V., Wilkie, K. & Pappa, R. 2004 Development of Modal Test Techniques for Validation of a Solar Sail Design, 45th AIAA/ASME/ASCE/AHS/ASC Structures, Structural Dynamics & Materials Conference. Structures, Structural Dynamics, and Materials and Co-located Conferences, American Institute of Aeronautics and Astronautics, Reston, VA, USA. (doi:10.2514/6.2004-1665)
[20] D Lobitz, J Grossman, J Allen, T Rice, C Liang, and F Davidson. Shape control of solar collectors using shape memory alloy actuators, 36th Structures, Structural Dynamics and Materials Conference, Structures, Structural Dynamics, and Materials and Co-located Conferences, () http://dx.doi.org/10.2514/6.1995-1117
[21] Chen Qin, Natale Don, Neese Bret et al. Piezoelectric Polymers Actuators for Precise Shape Control of Large Scale Space Antennas. SPIE Smart Structures and Materials and Nondestruvtive Evaluation and Health Monitoring, 18-22 Mar. 2007, San Diego, CA, United States
[22] Ruggiero, E. J. & Inman, D. J. 2009 Modeling and vibration control of an active membrane mirror, Smart Materials and Structures, 18(9), pp. 095027. (doi:10.1088/0964-1726/18/9/095027)
[23] Patterson, K., Pellegrino, S. & Breckinridge, J. 2010 Shape correction of thin mirrors in a reconfigurable modular space telescope, Proc. SPIE 7731, Space Telescopes and Instrumentation 2010: Optical, Infrared, and Millimeter Wave, 773121 (August 10, 2010), International Society for Optics and Photonics, pp. 773121-773121-12. (doi:10.1117/12.861442)
[24] Borggrafe, A., Heiligers, J., Ceriotti, M. & McInnes, C. R. 2014 Inverse Problem for Shape Control of Flexible Space Reflectors using Distributed Solar Pressure, Smart Mater. Struct., 23(7), 075026. (doi: 10.1088/0964-1726/23/7/075026)
[25] McInnes, C. R. 1999 Solar Sailing: Technology, Dynamics and Mission Applications, Springer-Praxis Series in Space Science and Technology, pp. 1-55. Berlin: Springer.